

PSR J1227–6208 and its massive white dwarf companion: pulsar emission analysis, timing update and mass measurements

Miquel Colom i Bernadich^{1*}, Vivek Venkatraman Krishnan^{1*}, David J. Champion¹, Paulo C. C. Freire¹,
Michael Kramer¹, Thomas M. Tauris^{2,1}, Matthew Bailes³, Alessandro Ridolfi^{4,1}, and Maciej Serylak^{5,6}

¹ Max-Planck-Institut für Radioastronomie, Auf dem Hügel 69, D-53121 Bonn, Germany

² Dept. of Materials and Production, Aalborg University, DK-9220 Aalborg Øst, Denmark

³ INAF – Osservatorio Astronomico di Cagliari, via della Scienza 5, 09047 Selargius (CA), Italy

⁴ Centre for Astrophysics and Supercomputing, Swinburne University of Technology, P.O. Box 218, Hawthorn, Vic, 3122, Australia

⁵ SKA Observatory, Jodrell Bank, Lower Withington, Macclesfield, SK11 9FT, United Kingdom

⁶ Department of Physics and Astronomy, University of the Western Cape, Bellville, Cape Town, 7535, South Africa

*e-mail: mcbernadich@mpi.fr-bonn.mpg.de, vkri.shnan@mpi.fr-bonn.mpg.de

Received ; accepted

ABSTRACT

PSR J1227–6208 is a 34.53-ms recycled pulsar with a massive companion. This system has long been suspected to belong to the emerging class of massive recycled pulsar–ONeMg white dwarf systems such as PSR J2222–0137, PSR J1528–3146 and J1439–5501. Here we present an updated emission and timing analysis with more than 11 years of combined Parkes and MeerKAT data, including 19 hours of high-frequency data from the newly installed MeerKAT S-band receivers. We measure a scattering timescale of 1.22 ms at 1 GHz with a flat scattering index $3.33 < \beta < 3.62$, and a mean flux density of 0.53 – 0.62 mJy at 1 GHz with a steep spectral index $2.06 < \alpha < 2.35$. Around 15% of the emission is linearly and circularly polarised, but the polarisation angle does not follow the rotating vector model. Thanks to the sensitivity of MeerKAT, we successfully measure a rate of periastron advance of $\dot{\omega} = 0.0171(11) \text{ deg yr}^{-1}$, and a Shapiro delay with an orthometric amplitude of $h_3 = 3.6 \pm 0.5 \mu\text{s}$ and an orthometric shape of $\zeta = 0.85 \pm 0.05$. The main source of uncertainty in our timing analysis is chromatic correlated dispersion measure noise, which we model as a power law in the Fourier space thanks to the large frequency coverage provided by the Parkes UWL receiver. Assuming general relativity and accounting for the measurements across all the implemented timing noise models, the total mass, companion mass, pulsar mass and inclination angle are constrained at $2.3 < M_i/M_\odot < 3.2$, $1.21 < M_c/M_\odot < 1.47$, $1.16 < M_p/M_\odot < 1.69$ and $77.5 < i/\text{deg} < 80.3$. We also constrain the longitude of ascending node to either $\Omega_a = 266 \pm 78 \text{ deg}$ or $\Omega_a = 86 \pm 78 \text{ deg}$. We argue against a neutron star nature of the companion based on the very low orbital eccentric of the system ($e = 1.15 \times 10^{-3}$), and instead classify the companion of PSR J1227–6208 as a rare, massive ONeMg white dwarf close to the Chandrasekhar limit.

Key words. (stars:) binaries: general – stars: neutron – stars: white dwarfs – stars: evolution – stars: fundamental parameters – stars: individual:: PSR J1227–6208

1. Introduction

The Chandrasekhar limit of white dwarf (WD) masses is a topic of ongoing research in astrophysics and theoretical physics. Studies show that maximally-rotating rigid WDs could sustain masses up to $M_{\text{WD}} \approx 1.48 M_\odot$ (Yoon & Langer 2005), but several effects have been speculated to allow them to exist beyond this limit, such as differential rotation (Yoon & Langer 2005) or high magnetisation (Kundu & Mukhopadhyay 2012), and Super-Chandrasekhar masses have been inferred indirectly from some Type Ia supernovae (Tomaschitz 2018). Additionally, extensions or modifications of general relativity (GR) must incorporate a prediction for the upper mass limit of WDs (e.g. Gregoris & Ong 2023; Mathew & Nandy 2021). To test these postulations, the empirical measurement of WD masses close to the Chandrasekhar limit is required. However, WDs with $M_{\text{WD}} \gtrsim 1.3 M_\odot$ are a rarity in the Galactic field. One of their windows of study is optical photometry, which has enabled the characterisation of their masses based on emission models (e.g. Caiazzo et al. 2021; Hollands et al. 2020; Külebi et al. 2010; Miller et al. 2023; Pshirkov et al. 2020). The other window of study are mass measurements of binary radio pulsars with massive WD com-

panions obtained via pulsar timing. This technique allows for the measurement of relativistic effects in the orbital motion and in the light propagation time; these are quantified by the post-Keplerian (PK) parameters. Under the assumption of GR, such measurements can result in the precise measurement of the WD and pulsar masses (Lorimer & Kramer 2005).

Timing measurements of pulsars with massive WD companions are relevant not only for probing the Chandrasekhar limit, but also for testing binary evolution and fundamental physics. In recycled pulsar binaries, we can test how binary interaction affects the resulting WD and NS mass distribution (for general insights on binary evolution and pulsar recycling, see Tauris & van den Heuvel 2023). For instance, there is a bi-modality in the WD mass distribution, with $M_{\text{WD}} \lesssim 0.5 M_\odot$ WDs being found with fully recycled pulsars at and $M_{\text{WD}} \gtrsim 0.7 M_\odot$ with mildly recycled pulsars (McKee et al. 2020; Shamohammadi et al. 2023). This divide is well understood thanks to models of binary evolution (Lazarus et al. 2014; Tauris et al. 2012; Tauris & van den Heuvel 2023), but the upper end of the WD mass distribution ($M_{\text{WD}} \gtrsim 1.1 M_\odot$) remains relatively unsampled. The birth NS mass distribution can also be directly sampled in these kind of

systems given the little mass accretion occurring during recycling (e.g. Lazarus et al. 2014; Cognard et al. 2017). For instance, the measurement of a pulsar mass of $M_p = 1.831(10) M_\odot$ in PSR J2222–0137 (Guo et al. 2021) is evidence that NSs can be born massive (heavier than $1.4 M_\odot$) instead of acquiring large amounts of extra mass via accretion (Cognard et al. 2017). Furthermore, the NS mass distribution is a probe of the physics of matter under conditions of extreme density (e.g. Özel & Freire 2016; Fonseca et al. 2021; Hu et al. 2020). Finally, in the most compact systems, timing of pulsars with WD companions also provides extremely precise tests of gravity theories (e.g., Voisin et al. 2020), as shown by the strict constraints on dipolar gravitational wave emission from PSR J2222–0137 (Guo et al. 2021), which have ruled out the phenomenon of spontaneous scalarisation predicted by some alternative gravity theories (Zhao et al. 2022).

As of today, only four pulsars with WD companions at the upper end of the mass distribution have been characterised. The most studied one is PSR J2222–0137, a 32.8-ms recycled pulsar in a circular 2.45-day orbit with a $M_{WD} = 1.319(4) M_\odot$ companion (Boyles et al. 2013; Cognard et al. 2017; Guo et al. 2021). With a parallax distance measured with long baseline interferometry of 268 pc (Deller et al. 2013; Guo et al. 2021), the lack of an optical detection implies a cold WD ($T < 3000$ K) with a cooling age of at least several Gyr (Kaplan et al. 2014). A similar case is PSR J1528–3146, a 60.8-ms recycled pulsar in a circular 3.18-day orbit with a $M_{WD} = 1.33^{+0.08}_{-0.07} M_\odot$ companion (Jacoby et al. 2006, 2007; Berthereau et al. 2023). In this case, the optical detection implies a cooling age between 1.5 and 3.2 Gyr (Jacoby et al. 2006), consistent with the pulsar characteristic age of 3.9 Gyr estimated by Berthereau et al. (2023). A third system is PSR J1439–5501, with a 28.6-ms pulsar in a 2.12-day orbit with a $M_{WD} = 1.27^{+0.14}_{-0.12} M_\odot$ optically detected companion with a cooling age of 0.1–0.5 Gyr (Jang et al., in prep. Faulkner et al. 2004; Lorimer et al. 2006; Pallanca et al. 2013). The final system is PSR B2303+46, with a young 0.937-s pulsar in a highly eccentric 12.34-day orbit with a $M_{WD} = 1.34^{+1.08}_{-0.15} M_\odot$ companion (Thorsett et al. 1993; Thorsett & Chakrabarty 1999). The WD companion is hot and young, implying a system age of 30 Myrs (van Kerkwijk & Kulkarni 1999).

In this work, we present a detailed study of PSR J1227–6208 (J1227–6208 from now on). Discovered independently by three different studies in data from the Murriyang Parkes telescope¹ (Bates et al. 2015; Knispel et al. 2013; Mickaliger et al. 2012), it is a 34.5-ms mildly recycled pulsar in orbit with a massive companion. With an orbital period of $P_b = 6.72$ days and a projected semimajor axis of $x = 23.2$ light seconds (ls), it has a high mass function of $f_M = 0.297 M_\odot$. Assuming a pulsar mass $M_p = 1.35 M_\odot$, this leads to a minimum companion mass of $M_c > 1.27 M_\odot$. Its low orbital eccentricity ($e = 1.15 \times 10^{-3}$) makes the possibility of a NS companion unlikely, giving more weight to a massive WD hypothesis instead. However, owing to the low orbital eccentricity, and large timing uncertainties, precise measurements of PK parameters in this system have been impossible until now.

It is for these reasons that the system was included in the Relativistic Binary program (RelBin, Kramer et al. 2021) of MeerTIME (Bailes et al. 2020), a large science project that takes advantage of the much higher timing precision of Southern pulsars made possible by the superb sensitivity of the MeerKAT telescope² (Jonas & MeerKAT Team 2016). The RelBin project

is designed to measure masses and test theories of gravity in 25 selected binary pulsar systems (Kramer et al. 2021), which includes J1227–6028. The updated timing analysis of J1227–6028 presented here includes a decade-long timing baseline of Parkes/Murriyang observations and two years of dedicated MeerKAT observations. This is the first timing experiment to include data from the newly commissioned S-band MeerKAT receivers (Barr 2018).

This paper is structured as follows. Section 2 details the observations used in this study and the data reduction for timing. Section 3 reports the emission study, including the modelling of the profile, scattering and spectral measurements, and the detection of polarised light. Section 4 reports the timing analysis, including the modelling of several timing noises, constraints on PK parameters, mass measurements and an exploration of the orbital orientation. Section 5 discusses the astrophysical implications of our measurements. In Section 6 we outline future prospects and lines of action for the study of this system. Finally, Section 7 concludes the paper and summarizes the key aspects of our measurements and discussions.

2. Data acquisition and reduction

2.1. Parkes/Murriyang

Table 1 shows the four data sets used in this work. Observations were performed first with the central beam of the 21-cm multibeam receiver (Staveley-Smith et al. 1996) and later with the ultra wide-bandwidth low-frequency receiver (UWL, Hobbs et al. 2020). The multibeam data set provides the longest baseline for the measurement of secular variations of the Keplerian parameters, while the UWL observations are particularly useful for constraining the dispersion measure (DM) evolution due to their overlap with the MeerKAT observations and their very large bandwidth. UWL observations also include three dense orbital campaigns on the dates of 4–10 October 2020, 20–26 July 2022 and 3–9 May 2023, with 7 observations each, accumulating 5.74, 10.41 and 17.63 hours each. These campaigns have two aims: aiding in the measurement of the time delay of the pulses as they propagate through the gravitational field of the companion (Shapiro delay, Shapiro 1964) and constraining DM evolution within a single orbit. In line with this objective, the first of the orbital campaign was coordinated with the MeerKAT orbital campaign with the L-band receivers (Section 2.2) so that observations alternate each other.

The multibeam receiver data were recorded by the Center for Astronomy Signal Processing and Electronics Research (CASPER) Parkes Swinburne Recorder (CASPSR, Sarkissian et al. 2011) backend. The data were folded with 512 frequency channels, four polarisation channels, 1,024 phase bins and with coherent de-dispersion at $DM \approx 363 \text{ cm}^{-3} \text{ pc}$. Each observation was accompanied by a noise-diode observation for polarisation calibration. Calibration was performed on each file with the `pac` command from the PSRCHIVE³ software package (Hotan et al. 2004). The archives were manually excised of radio-frequency-interference (RFI) with the PSRCHIVE/`pazi` interface, and the 80 bottom channels and 32 top channels were zero-weighted with the PSRCHIVE/`paz` command to remove Gaussian noise caused by the loss of sensitivity at the edge of the bandpass. The bands were then scrunched to four frequency sub-bands, a single intensity channel and a single subintegration per observation with the PSRCHIVE/`pam` command for the production

¹ <https://www.parkes.atnf.csiro.au/>

² <https://www.sarao.ac.za/science/meerkat/about-meerkat/>

³ <https://psrchive.sourceforge.net/>

Table 1. Summary of the data sets used in this analysis.

Receiver(s)	Freq. (MHz)	Bandw. (MHz)	Temp. K	Gain K Jy^{-1}	# obs	Time (hours)	First obs.	Last obs.	# bands	# ToAs (μs)	Median err.
Parkes multibeam	1382	400	~ 21	~ 0.9	93	33	1 March 2012	8 April 2019	4	365	26.4
MeerKAT L-band	1284	856	4–7	~ 2.6	37	26	12 February 2019	25 May 2023	8	508	5.39
Parkes UWL	2368	3328	~ 22	~ 0.9	56	72	4 May 2020	6 June 2023	8	444	19.5
MeerKAT S-band	2406	875	4–7	~ 2.3	10	19	12 May 2023	28 May 2023	4	228	5.43

Notes. The data were recorded in folding mode with four polarisation channels and 1,024 phase bins of 28.28 of μs in length. The system temperatures are drawn from the MeerKAT General documentation, the Multibeam Receiver Description webpage and (Hobbs et al. 2020). The gain is estimated from the collecting area, accounting that only 56 antennas are available in the MeerKAT S-band configuration. The last three columns indicate timing data reduction parameters: number of sub-bands used in multi-frequency timing, number of ToAs per data set, and the median ToA uncertainty.

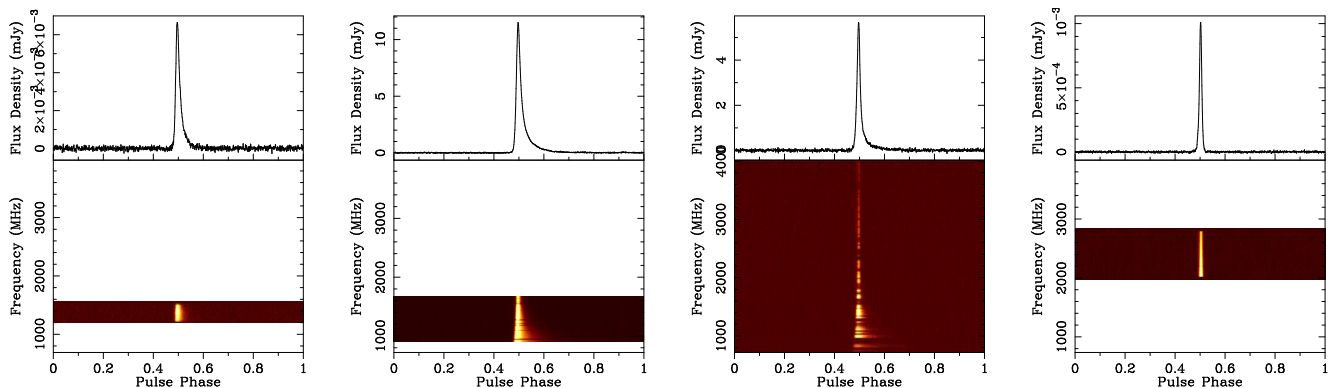


Fig. 1. Time-integrated pulse profiles of J1227–6208 as recorded with the different receivers (from left to right: Parkes multibeam, MeerKAT L-band, Parkes UWL and MeerKAT S-band). The top plots show the intensity of the integrated emission, while the bottom plots are frequency-resolved. Only the MeerKAT L-band and Parkes UWL data sets are flux calibrated. The plots were made with PSRCHIVE/psrplot.

of frequency-resolved times of arrival (ToAs). To derive timing templates for each band, we obtained a frequency-resolved standard profile resulting from the time integration of all multi-beam CAPSR observations (with the exclusion of three heavily RFI-affected observations) into a single rotational phase cycle. The analytic timing templates were then produced for each sub-band by fitting a combination of von Mises functions with PSRCHIVE/paas program. The ToAs were produced with the PSRCHIVE/pat command using the FDM algorithm with the two-dimensional, frequency-resolved timing template, where each subintegration resulted a ToA from each of the four sub-bands.

The UWL receiver data were recorded by the Medusa cluster (Hobbs et al. 2020) with 3,328 frequency channels, four polarisation channels, 1,024 phase bins and with coherent de-dispersion at $\text{DM} \approx 363 \text{ cm}^{-3} \text{ pc}$. In addition, the data were also recorded with real-time folding based on an early pulsar ephemeris. The data were processed using the psrpye processing pipeline⁴. This pipeline carries out flux and polarization calibration, and also automatically removes RFI using c1fd⁵. It results in data that is cleansed of RFI, calibrated, and broken down into various time, frequency, and polarization resolutions. The RFI excision step also excises a standard set of frequencies, on top of whichever part of the data that the algorithm considers to be contaminated. These frequency sets were decided based on the knowledge of the known transmitter frequencies that routinely affect the data. To boost the quality of ToAs, the data was scrunched into full intensity, eight frequency channels and

subintegrations of two hours in length with the PSRCHIVE/pam command. The ToAs were produced with the PSRCHIVE/pat command using the FDM algorithm. Analogously to the multi-beam CASPSR data set, the timing template was modelled with PSRCHIVE/paas from the integration of all of the files into a 2-dimensional frequency-resolved standard profile, with the exclusion of three severely RFI-affected observations.

2.2. MeerKAT

The MeerKAT data sets provide the most precise ToAs owing to the large sensitivity of the telescope. Most of the data were recorded with the L-band receivers (26 hours, 856–1712 MHz), but 19 hours were recorded with the new S-band receivers in the S1 configuration (1968–2843 MHz, Barr 2018) on 12–28 May 2023 to ensure a measurement of the Shapiro delay with a significant reduction of DM noise (see Table 1). The data were recorded with the pulsar timing user-supplied equipment (PTUSE, Bailes et al. 2020) machines as part of the MeerTIME science program (Bailes et al. 2020), and included an orbital campaign on the dates of 4–11 October 2020 that accumulated 13 hours over nine L-band observations, with a dedicated five-hour-long observation at superior conjunction on 11 October 2020, aimed at constraining the Shapiro delay.

Both data sets were recorded with 1,024 frequency channels, four polarisation channels and coherent dedispersion at $\text{DM} \approx 363 \text{ cm}^{-3} \text{ pc}$. The L-band data were processed, cleaned of RFI and calibrated with the meerpipeline⁶, which re-

⁴ <https://github.com/vivekvenkris/psrpye>

⁵ <https://github.com/v-morello/c1fd>

⁶ <https://zenodo.org/records/7961071>

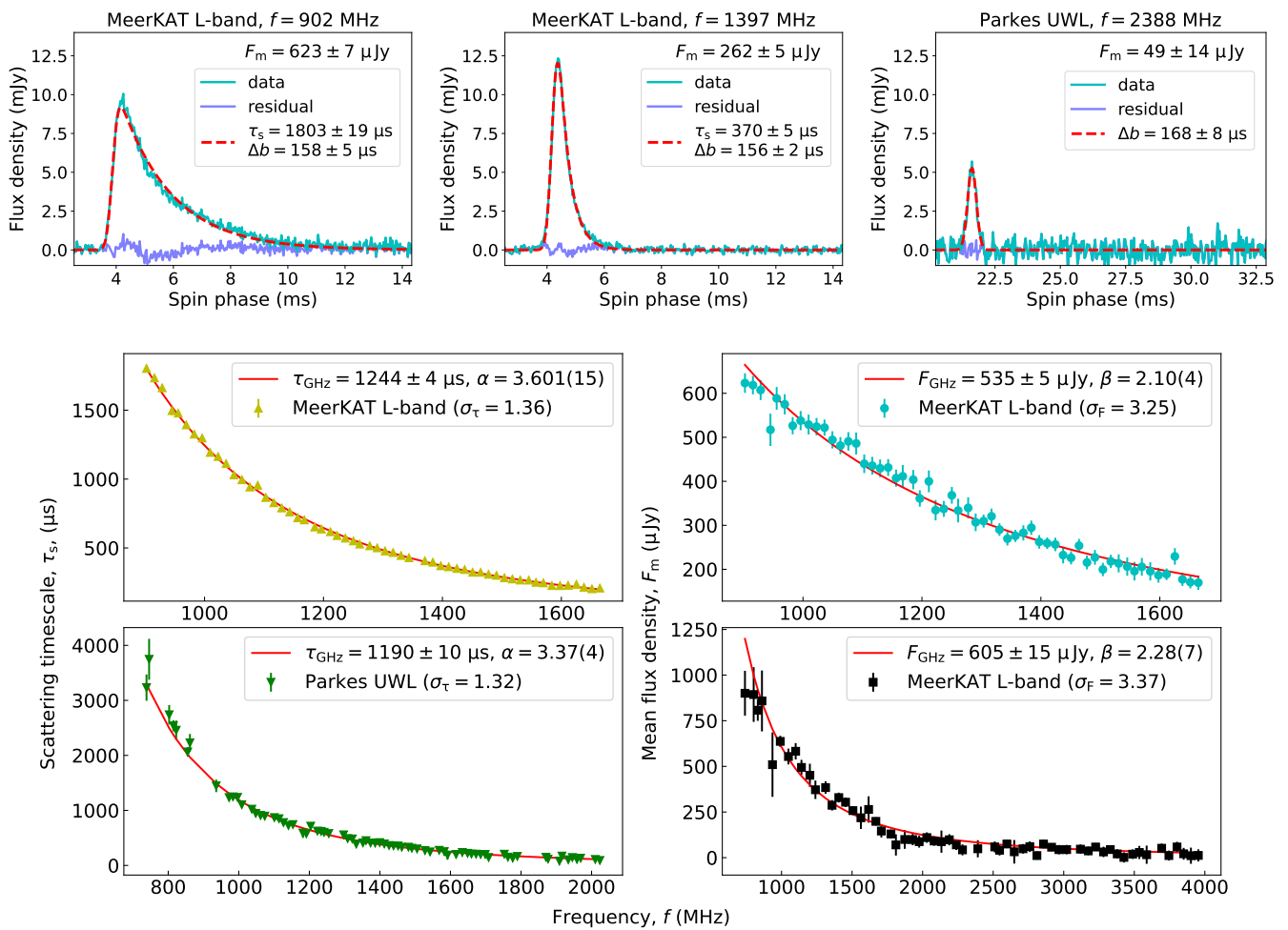


Fig. 2. Top: pulse profiles of J1227–6208 at $f = 902$ MHz and $f = 1397$ MHz as seen by the MeerKAT L-band receiver (left and middle plots), and at $f = 2388$ MHz as seen by the Parkes UWL receiver (right plot). The data (cyan lines) is shown against the best model (red dashes, fitted with equation 1) and the fit residuals (blue lines). The fit parameters τ_s and Δb from equation (1), and the mean flux density F_m are quoted on each profile. **Bottom:** measurements of $\Delta\tau$ and F_m at each frequency on the MeerKAT L-band and Parkes UWL profiles (dots with uncertainties), and the best fits of the power laws (2) and (3) (red lines). The data points are displayed accounting for the error factors σ_τ and σ_F , and the relevant τ_{GHz} , α , F_{GHz} and β values are quoted in the legend.

sulted in the trimming of the outer edges, leaving only 926 channels of useful data with a bandwidth of 775.5 MHz. Any remaining RFI was manually removed with the PSRCHIVE/paz command. Observations were then fully summed in polarization, and scrunched into eight frequency channels and 20-min-long subintegrations to extract frequency-resolved ToAs with the PSRCHIVE/pat command. Analogous to the Parkes data sets (Section 2.1), the frequency-resolved timing template was derived using the PSRCHIVE/paas on frequency-resolved standard profiles resulting from the time integration of the observations in the October 4–11 October 2020 orbital campaign. Unfortunately, calibration files were not available for the S-band data set, as it was taken jointly with commissioning data, and therefore it could not be calibrated nor band-pass corrected. This, however, is unlikely to affect our timing precision. S-band data were cleaned of RFI with the c1fd software, and it was sub-banded to four frequency channels for frequency-resolved timing, with the profile being created from the integration of all of the observations, following the same steps as the L-band data.

3. Emission analysis

3.1. Profile evolution

J1227–6208 suffers from significant scattering and has a steep flux density spectrum. Fig. 1 shows time-integrated, frequency-resolved standard profiles from the four different receivers listed in Table 1. The most obvious feature is scattering at the MeerKAT L-band and the bottom of the Parkes UWL band, resulting in an exponential, frequency-dependent tail of the pulse profile. In addition, the pulse brightness fades quickly at the top of the Parkes UWL band. It should be noted that the dark bands in the Parkes UWL profile are a result of the RFI excision processes, and are not intrinsic to the pulsar emission. To measure the scattering timescale τ_s at each frequency, we model the pulse at a given frequency f as a single Gaussian function convolved with a scattering exponential tail

$$S_b = \int A \times \exp\left(\frac{(b' - b_0)^2}{2 \times \Delta b^2}\right) \times \exp\left(-\frac{b - b'}{\tau_s}\right) db', \quad (1)$$

where b is the spin phase in bins, and b_0 and Δb stand for the Gaussian center and standard deviation. We measure the scattering index α by fitting the evolution of τ_s as a power law function

of f ,

$$\tau_s(f) = \tau_{\text{GHz}} \left(\frac{f}{\text{GHz}} \right)^{-\alpha}, \quad (2)$$

where τ_{GHz} is the reference value at $f = 1$ GHz. For the flux density spectral index β , we measure the mean flux density F_m across the pulse phase at each sub-band, deriving the uncertainty from the off-pulse baseline noise, and fit another power law

$$F_m(f) = F_{\text{GHz}} \left(\frac{f}{\text{GHz}} \right)^{-\beta}, \quad (3)$$

where F_{GHz} is the reference value at $f = 1$ GHz.

We perform least- χ^2 fits of equations (1),(2) and (3) on the frequency-resolved, time-integrated MeerKAT L-band and Parkes UWL profiles (second and third plots in Fig. 1) with the python module `scipy` (Virtanen et al. 2020). As shown in the upper part of Fig 2, the scattered Gaussian modelling of the profile adjusts well to the data, with only some minor residual structure after subtraction of the model. The intrinsic pulse width stays consistent at $150 < \Delta b < 170 \mu\text{s}$ across the whole band, and the parameter τ_s becomes redundant in the modelling of the pulse at $f > 2$ GHz in the Parkes UWL dataset, where a simple Gaussian function provides an adequate description. Thus, we restrict the measurement of τ_{GHz} and α at $f < 2$ GHz. To ensure a proper uncertainty estimation on the scattering and spectral parameters, we multiply the individual measurement uncertainties of τ_s and F_m by the error factors σ_τ and σ_F ($\delta' = \sigma \times \delta$, where δ is the set of measurement uncertainties). Subsequently, we tune the values of σ_τ and σ_F to achieve a reduced $\chi^2 = 1$ in the fit of equations (2) and (3).

Our fits confirm the steep spectrum of J1227–6208 and measure a scattering index $\alpha < 4$. The lower part of Fig. 2 shows the fit parameters for τ_{GHz} , α , F_m and β from equations (2) and (3) on the measurements of τ_s and F_m in the MeerKAT L-band and Parkes UWL datasets. The power law describes τ_s accurately for the MeerKAT L-band data set, with $\tau_{\text{GHz}} = 1244 \pm 4 \mu\text{s}$ and $\alpha = 3.601(15)$. However, this is different from the measurement performed in the Parkes UWL profile, which results in $\tau_{\text{GHz}} = 1190 \pm 10 \mu\text{s}$ and $\alpha = 3.37(15)$. The difference likely comes from the different frequency coverage and the low quality of measurements at $f < 900$ MHz. Nonetheless, both fits agree on $\alpha < 4$, far from the $\alpha = 4.4$ predicted from a Kolmogorov medium and the $\alpha = 4$ from Gaussian inhomogeneities (Rickett 1977; Romani et al. 1986), as already seen in some pulsars behind complex ISM environments (e.g. Löhmer et al. 2004; Krishnakumar et al. 2019; Oswald et al. 2021). On the other hand, our F_m measurements are not as precise, as indicated by the $\sigma > 3$ values. The most likely explanation is the lower S/N of the Parkes standard profiles due to its lower gain and the large degree of zapping of frequency channels during RFI excision. Nonetheless, both the MeerKAT L-band and Parkes UWL agree on a very steep spectrum, with $\beta = 2.10(4)$ and $\beta = 2.28(7)$, respectively, on the steeper side the typically observed values of $\beta = 1.4 \pm 1.0$ (Bates et al. 2013). The derived reference flux densities are $F_{\text{GHz}} = 535 \pm 5 \mu\text{Jy}$ and $F_{\text{GHz}} = 605 \pm 15 \mu\text{Jy}$. Regarding the peak flux density, the combined effect of scattering and spectral behaviour results in the brightest observed peak flux density of 13–14 mJy -and highest S/N - at $f \approx 1200 - 1300$ MHz.

3.2. Polarised emission

We perform a rotation measure (RM) fit on the MeerKAT L-band and Parkes UWL profiles with `PSRCHIVE/rmfit`, finding the maximum of integrated linearly polarised flux density at

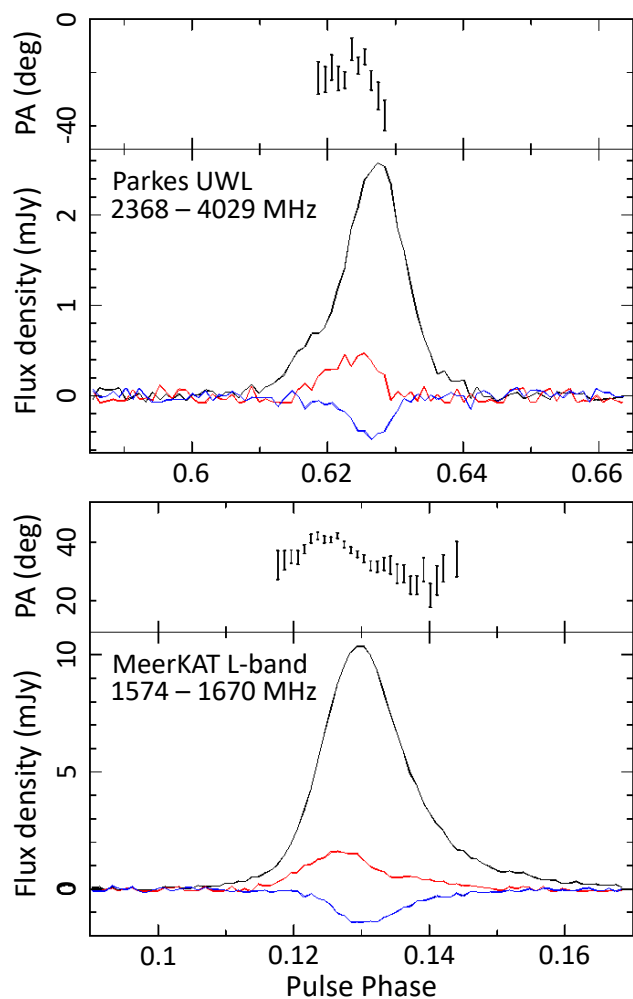


Fig. 3. Parkes UWL (top) and MeerKAT L-band (bottom) polarisation profiles of J1227–6208, RM-corrected at 47.3 rad cm^{-1} . Total flux density (black lines), linearly polarised intensity (red lines), circularly polarised intensity (blue lines) and the PA angle (black error bars) are plotted as a function of the pulse phase.

$\text{RM} = 47.7$ and 46.2 rad cm^{-1} , with half-widths full-maximums of 50 and 30 rad cm^{-1} , respectively. These two values are consistent with each other, and they imply an average magnetic field parallel to the line of sight (LOS) of $0.16 \mu\text{G}$. Fig. 3 shows the polarised emission of J1227–6208 at $f = 1574 - 1670$ MHz from the MeerKAT L-band profile, and at $f = 2368 - 4029$ MHz from the Parkes UWL profile. Approximately 15% of the total intensity is linearly polarised, and a similar fraction of circular polarisation is detected. Linear polarisation is more prominent in the first half of the pulse, peaking before the total intensity, while circular polarisation peaks along with the total intensity. The position angle (PA) of the linear polarisation shows an increase before the linearly polarised emission peaks, and a decrease afterwards, instead of following the rotating vector model from Radhakrishnan & Cooke (1969). In the MeerKAT L-band, scattering drags some of the polarised emission into the scattering tail, resulting in some spurious PA angle measurements towards the end of the pulse. In the Parkes data set, an extra feature of the profile is revealed at the beginning of the pulse, making it slightly asymmetric. This feature is coincident with the off-centre linearly polarised emission.

Table 2. Resulting noise models as derived by TEMPO2/TempoNEST.

Model	$\nu_{\text{cut,spin}}^{-1}$ (days)	$\nu_{\text{cut,DM}}^{-1}$ (days)	$\log E$	χ^2	$\log A_{\text{spin}}$	γ_{spin}	$\log A_{\text{DM}}$	γ_{DM}
L	...	100	16310.61(4)	1.013	-10.02	1.148
Ls	500	100	16387.3(1)	0.973	-11.71	1.485	-9.99	1.320
C	...	50	16326.21(8)	0.983	-10.09	1.113
Cs	100	50	16416.80(2)	0.966	-11.75	1.499	-10.01	1.573
VC	...	30	16329.1(2)	0.944	-10.09	1.432
VCs	30	30	16430.9(5)	0.932	-11.81	1.097	-10.04	1.307

Notes. The best-fit reduced χ^2 is derived from a subsequent TEMPO2 fit.

4. Timing analysis

4.1. Noise modelling

We fit the entire ToA time series with the DDH model, a modified version of the Damour-Deurelle timing model (DD, Damour & Deruelle 1986) which includes the orthometric parametrization of the Shapiro delay (Freire & Wex 2010). The fit itself was performed with the pulsar timing software TEMPO2⁷ (Edwards et al. 2006; Hobbs et al. 2006) and its plug-in TEMPO2/TempoNEST⁸, which implements multi-nested Bayesian sampling of the highly multidimensional space of the timing model, including the pulsar spin and astrometric parameters, the DM evolution, the five Keplerian parameters and five independent PK parameters. In addition, TEMPO2/TempoNEST also fits for Gaussian white noise and correlated red noise.

The ToA time series is affected by Gaussian instrumental noise and red spin and DM noise, which can significantly contaminate the measurement of other parameters in the timing model. In particular, there is a significant DM variability as measured in different observations, an effect that becomes very prominent in the MeerKAT L-band and Parkes UWL data sets. Following the method first described in van Haasteren et al. (2009), we model the presence of red noise as a power spectral density in the Fourier domain described with a power law

$$S(\nu) = A^2 \left(\frac{\nu}{\text{yr}^{-1}} \right)^{-\gamma}, \quad (4)$$

where $A = \{A_{\text{spin}}, A_{\text{DM}}\}$ is the dimensionless amplitude of the correlation matrix, ν is the spectral frequency and $\gamma = \{\gamma_{\text{spin}}, \gamma_{\text{DM}}\}$ is the power law index. We account for two possible sources of red noise: spin noise caused by the rotational variations originating within the pulsar, and DM noise originated by variations within the interstellar medium (ISM) along the LOS. The spin noise is frequency-independent (achromatic), while the DM noise is defined by its frequency dependence (chromatic), with

$$A_{\text{DM},f} = A_{\text{DM}} \times \left(\frac{f}{1,400 \text{ MHz}} \right)^{-2}, \quad (5)$$

where A_{DM} corresponds to the amplitude of red DM noise at $f = 1,400 \text{ MHz}$. To account for uncorrelated Gaussian (white) instrumental and pulsar noise for each telescope backend k (Section 2), we add the EQUAD $_k$ and EFAC $_k$ parameters that re-scale the ToA uncertainties σ_k into

$$\hat{\sigma}_k^2 = (\text{EFAC}_k \sigma_k)^2 + \text{EQUAD}_k^2, \quad (6)$$

⁷ <https://bitbucket.org/psrsoft/tempo2>

⁸ <https://github.com/LindleyLentati/TempoNest>

where k is specific to each telescope backend. As a starting point, TEMPO2/TempoNEST only requires the extra assumption of a cut-off frequency for the correlated noises as a user-given input. We performed six different TEMPO2/TempoNEST runs: half of them include white noise and red DM noise, while the other half also include red spin noise. Each of these runs has different noise cut-offs, chosen from $\nu_{\text{cut}}^{-1} = 30, 50, 100$ and 500 days. The resulting noise models, listed in Table 2, are named according to the cut-offs and inclusion or exclusion of red spin noise: loose (L), loose with spin (Ls), constrained (C), constrained with spin (Cs), very constrained (VC) and very constrained with spin (VCs).

All noise models provide an adequate description of the data, including those that do not include red spin noise, and red DM noise is always dominant over red spin noise when both are included. As shown in Table 2, models that include both noises are favoured by the nested importance sampling global log-evidence ($\log E$), and A_{DM} is two orders of magnitude larger than A_{spin} . That is not surprising, as J1227–6028 is a recycled pulsar with an expected high rotational stability, and it shows that the main source of timing noise is indeed the ISM. Furthermore, Table 2 also shows that models with shorter ν_{cut}^{-1} values are favoured by the $\log E$. Nonetheless, the resulting $\chi^2 < 0.95$ values for the VC and VCs models hint towards the possibility of over-fitting when accounting for large frequencies in the red noises.

4.2. PK parameters constraints

We fit five PK parameters to constrain the component masses and the effects of proper motion. These are the rate of periastron advance $\dot{\omega}$, the orthometric shape and range parameters of the Shapiro delay h_3 and ζ as defined in Freire & Wex (2010), the orbital period derivative \dot{P}_b and the projected semi-major axis derivative \dot{x} . From the preliminary timing solution, we expect $\dot{\omega}$ to be dominated by the relativistic precession of the Keplerian orbit as predicted by GR,

$$\dot{\omega} = 3 \left(\frac{P_b}{2\pi} \right)^{-5/3} \frac{(T_\odot M_t)^{2/3}}{1 - e^2}, \quad (7)$$

where the total system mass M_t is expressed in units of M_\odot , and $T_\odot = GM_\odot/c^3 = 4.92549094764 \mu\text{s}$ as defined in Prša et al. (2016). The Shapiro delay describes the periodic time delay of the pulses as they propagate through the gravitational field of the companion (Shapiro 1964). However, as its periodicity is equal to P_b , part of its signal is degenerate with the Rømer delay for systems with low inclination angles (i). Therefore, we use the orthometric parameters h_3 and ζ to model the residual unabsorbed component of the Shapiro delay instead (Freire & Wex 2010).

Table 3. Constraints on the PK parameters and the component masses from the global fits.

Noise model	$\dot{\omega}$ (deg yr ⁻¹)	h_3 (μ s)	ζ	\dot{P}_b $\times 10^{-13}$ s s ⁻¹	\dot{x} $\times 10^{-15}$ ls s ⁻¹	M_p (M_\odot)	M_c (M_\odot)	i (deg)
L	0.0171(9)	3.8(3)	0.84(4)	0.02 ± 2.4	-1.6 ± 6.6	1.58(11)	1.41(5)	79.2(6)
Ls	0.0173(8)	3.7(3)	0.84(3)	2.9 ± 2.3	-3.5 ± 6.5	1.59(10)	1.42(5)	78.6(7)
C	0.0170(9)	3.7(3)	0.85(3)	1.0 ± 2.6	-5.0 ± 6.9	1.53(11)	1.38(5)	79.3(7)
Cs	0.0171(8)	3.5(2)	0.86(3)	3.7 ± 2.5	-9.1 ± 7.2	1.53(10)	1.39(5)	78.4(7)
VC	0.0171(9)	3.6(3)	0.86(3)	1.0 ± 2.6	-3.7 ± 7.0	1.54(11)	1.39(5)	79.2(7)
VCs	0.0170(8)	3.4(2)	0.85(3)	4.6 ± 2.7	-6.5 ± 8.0	1.51(11)	1.38(5)	78.2(7)
extended	0.0171(11)	3.6(5)	0.85(5)	1.54(15)	1.40(7)	78.7 ± 1.2

Notes. The PK parameters were measured in a global fit with TEMPO2 under the assumption of the noise models derived by TEMPO2/TempoNEST (Table 2). The component masses and the inclination angle are derived from the χ^2 mapping of DDGR solutions (Section 4.3). The **extended** row shows comprehensive uncertainties accounting for all measurements across the different noise models.

The orthometric amplitude

$$h_3 = T_\odot M_c \left(\frac{1 - \cos i}{1 + \cos i} \right)^{3/2} \quad (8)$$

describes the amplitude of the unabsorbed component, which depends on the companion mass M_c and the inclination angle i , while the orthometric shape

$$\zeta = \left(\frac{1 - \cos i}{1 + \cos i} \right)^{1/2} \quad (9)$$

describes the shape of the delay in the orbital phase, depending only on i .

The remaining PK parameters, \dot{P}_b and \dot{x} , have the estimated GR contributions of $\dot{P}_b \sim 10^{-15}$ s s⁻¹ and $\dot{x} \sim 10^{-20}$ ls s⁻¹, but likely much more dominant contributions are those of the Galactic acceleration field and the proper motion. For \dot{P}_b , we expect the Shklovskii effect and the Galactic acceleration field to be the dominant contributors (Shklovskii 1970; Damour & Taylor 1991), which introduce a derivative based on the Doppler factor (D) derivatives:

$$\frac{\dot{P}_b}{P_b} = - \left(\frac{\dot{D}}{D} \right)_{\text{Shkl}} - \left(\frac{\dot{D}}{D} \right)_{\text{Gal}} = \frac{1}{c} [|\boldsymbol{\mu}|d + \mathbf{K}_0(\mathbf{a}_{\text{PSR}} - \mathbf{a}_{\text{SSB}})] \quad (10)$$

where $\boldsymbol{\mu} = (\mu_{\text{RA}}, \mu_{\text{DEC}})$ is the sky proper motion of the pulsar, \mathbf{K}_0 is the Solar System barycenter (SSB) to pulsar system unit vector and \mathbf{a}_{PSR} and \mathbf{a}_{SSB} are the Galactic acceleration field measured at the pulsar system and the SSB, respectively. On the other hand, the contribution to \dot{x} is expected to be dominated by the geometric effect introduced by the proper motion of the system on the sky (Kopeikin 1996):

$$\frac{\dot{x}}{x} = 1.54 \times 10^{-16} \cot i \left(-\frac{\mu_{\text{RA}}}{\text{mas yr}^{-1}} \sin \Omega_a + \frac{\mu_{\text{DEC}}}{\text{mas yr}^{-1}} \cos \Omega_a \right), \quad (11)$$

where Ω_a is the longitude of ascending node. Finally, we do not include the amplitude of the Einstein delay γ_E , as for circular systems like J1227–6208 it is expected to be highly degenerate with \dot{x} , and its inclusion would lead to the non-detection of \dot{x} instead (see Ridolfi et al. 2019 for a detailed discussion of this phenomenon).

To measure the PK parameters, we assume the noise models found by TEMPO2/TempoNEST and perform a global re-fit of

all model parameters with TEMPO2. We quote the fit values and 1σ uncertainties as reported by the least- χ^2 TEMPO2 fit, which are consistent with the ones reported by TEMPO2/TempoNEST but with slightly larger uncertainties. We choose this because the TEMPO2 fits are more consistent across noise models, and because it provides a more conservative uncertainty estimate. Additionally, it is consistent with the use of TEMPO2 in the mass measurements presented in the following sections.

The measured PK parameters are consistent across all noise models. Table 3 presents the measured value of each PK parameter for each assumed noise model in the global fit. The rate of periastron advance presents a very consistent value of $\dot{\omega} = 0.0171(11)$ deg yr⁻¹ if we consider extended uncertainties from all of the measurements listed in Table 3, which results in a $\sim 15\sigma$ detection and indicates a total system mass of $M_t = 2.9 \pm 0.3 M_\odot$. The Shapiro delay parameters $h_3 = 3.6 \pm 0.5 \mu$ s and $\zeta = 0.85 \pm 0.05$ are measured with high significance for the first time, presenting $\sim 7\sigma$ and $\sim 17\sigma$ detections if we consider extended uncertainties from across all the noise models.

The red DM noise is a major source of uncertainty in our measurement. The parameters most affected by the choice of the noise model is h_3 , ranging from 3.8(3) μ s in the **L** model to 3.4(2) μ s in the **VCs**. In general, we measure lower values in models with high-frequency cut-offs and with both spin and DM noise. A possible explanation is that unmodelled red noise can bias the Shapiro delay measurement to higher amplitude values, especially achromatic spin noise. A similar phenomenon can occur in the opposite direction, with noise models removing power from the Shapiro delay signal when the orbital period is close to ν_{cut} . That may be a potential explanation for the $\chi^2 < 0.95$ value in the **VC** and **VCs** models (Table 2). Nonetheless, the measured PK values of all parameters are consistent across all noise models within the 1σ uncertainty ranges.

The MeerKAT data set dominates the measurement of the orthometric Shapiro delay parameters. Fig. 4 shows the timing residuals as a function of the orbital phase under the assumption of the **Cs** noise model. Despite some small gaps in orbital coverage, only the MeerKAT-derived ToAs have enough precision to detect the Shapiro delay with high significance, and therefore to constrain the component masses in this system. To corroborate this, we have attempted to fit the h_3 and ζ parameters on each ToA dataset. The MeerKAT L-band ToAs reproduce the measurement from the global fit, while the S-band ToAs yield only a slight loss of precision owing to the sparser orbital coverage. On the other hand, the Parkes multibeam data set provides only

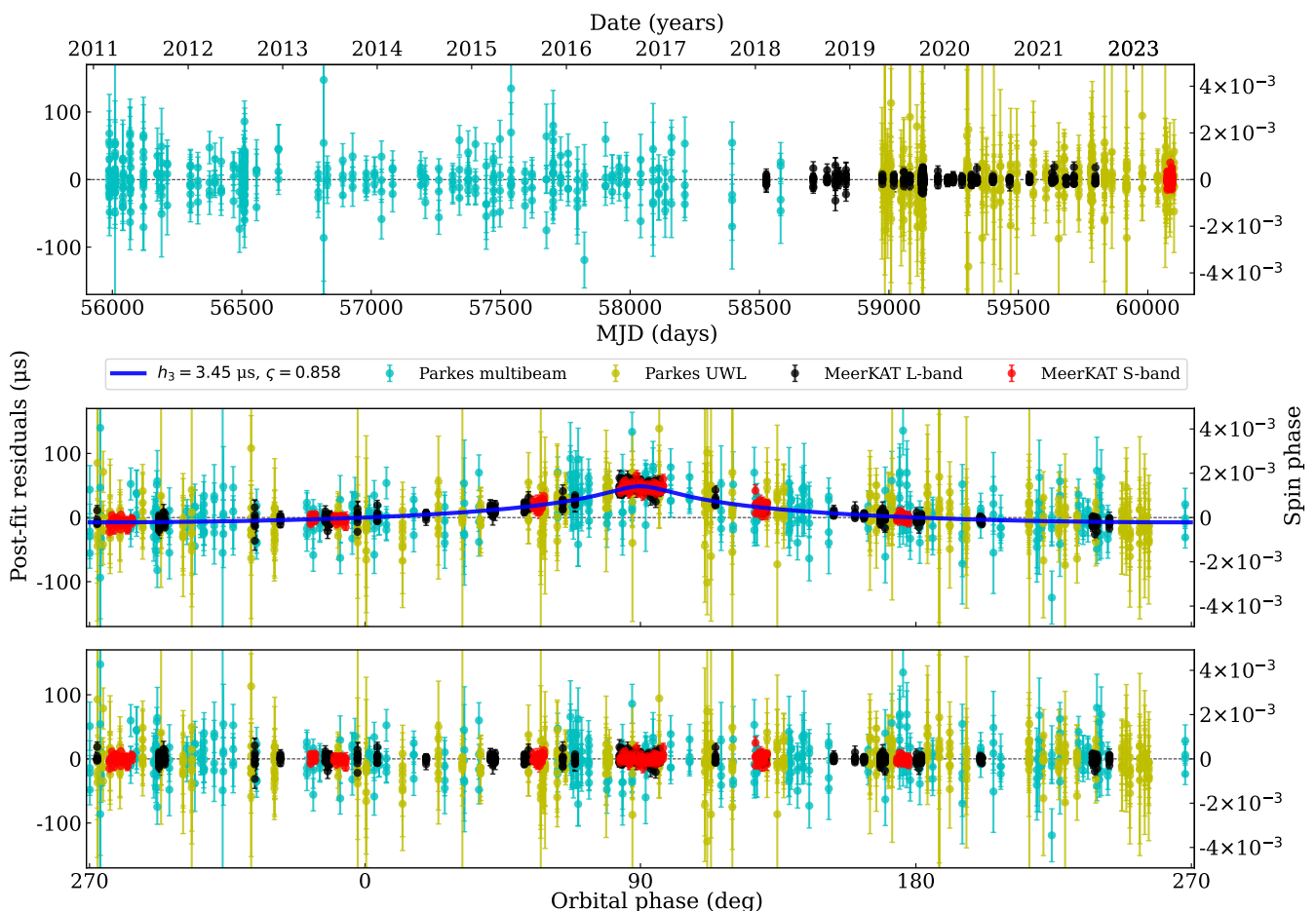


Fig. 4. **Top:** ToA residuals as a function of MJD under the assumption of the Cs noise model, showing flat, Gaussian residuals. **Middle:** ToA residuals as a function of the orbital phase (orbital position from the ascending node, true anomaly + periastron) excluding the h_3 and ζ parameters from the timing model, showing the full amplitude of the Shapiro delay signal. The continuous blue line depicts the predicted Shapiro delay described by $h_3 = 3.45 \mu\text{s}$ and $\zeta = 0.858$. **Bottom:** the orthometric Shapiro delay parameters are now included in the model, resulting in flat, Gaussian residuals.

very loose constraints as discussed in Section 4.4 and the Parkes UWL dataset is unable to converge on significant values.

The two remaining PK parameters, \dot{P}_b and \dot{x} , do not yield a significant detection with the current timing baseline but still offer useful constraints. Table 5 presents the values for all the timing parameters of the global fit using the Cs noise model, as well as the expected contributions to \dot{P}_b and \dot{x} . The DM-derived distance from the NE2001 (Cordes 2004) and YMW16 (Yao et al. 2017) electron density models are $d = 8.3$ kpc and $d = 8.5$ kpc, respectively. With the detected proper motion vector of $\mu = (-6.1 \pm 0.3, 0.41 \pm 0.36) \text{ mas yr}^{-1}$ and the Galactic gravitational potential from McMillan (2017) in eq. (10), we predict an order of magnitude of $\dot{P}_b \sim 10^{-13} \text{ s s}^{-1}$. Likewise, assuming an inclination angle of $i \approx 79$ deg (Section 4.3) in equation (11), we predict a maximum value of $|\dot{x}_{\text{max}}| \approx 4.2 \times 10^{-15} \text{ ls s}^{-1}$ in case of a favourable Ω_a value. These estimates are of the same order of magnitude as the constraints on \dot{P}_b and \dot{x} presented in Table 3, which also present a consistent sign across all noise models, suggesting that the constraints can provide some physical information. Taking this into account, in Section 4.5 we translate the constraint on \dot{x} into constraints on the orbital geometry of the system, and in Section 4.6 we discuss the possible implications of the \dot{P}_b constraints for the measurement of the spin period derivative \dot{P}_s .

4.3. Mass constraints

In a common Bayesian approach (e.g. Splaver et al. 2002), we enforce the consistency of the PK parameters with GR and derive constraints on the pulsar mass M_p , the companion mass M_c and the inclination angle i . We use the DDGR model, a modified version of the DD model that implements the PK effects directly from M_t and M_c as predicted by GR (Taylor & Weisberg 1989). This allows us to explore a two-dimensional space of parameters to constrain the mass components and orbital inclination. For each noise model derived by TEMPO2/TempoNEST, we perform TEMPO2 fits with the DDGR model in a uniform grid in the $M_t - \cos i$ space, where the uniform spacing on $\cos i$ is chosen to achieve a uniform sampling of the possible orbital geometries of the system. At each point in the grid, we register the resulting χ^2 and transform it into a probability value, deriving a likelihood distribution. Subsequently, the distribution is integrated into marginal one-dimensional probability distributions for M_p , M_c and i . Given that \dot{P}_b and \dot{x} are influenced by the proper motion of J1227-6208 and the Galactic acceleration field, we include them as independent excess parameters that do not need to be consistent with GR.

The values of M_p , M_c and i , listed in Table 3, are consistent across all noise models, but there is some tension between the DDGR constraints and the ζ parameter. Fig. 5 depicts the

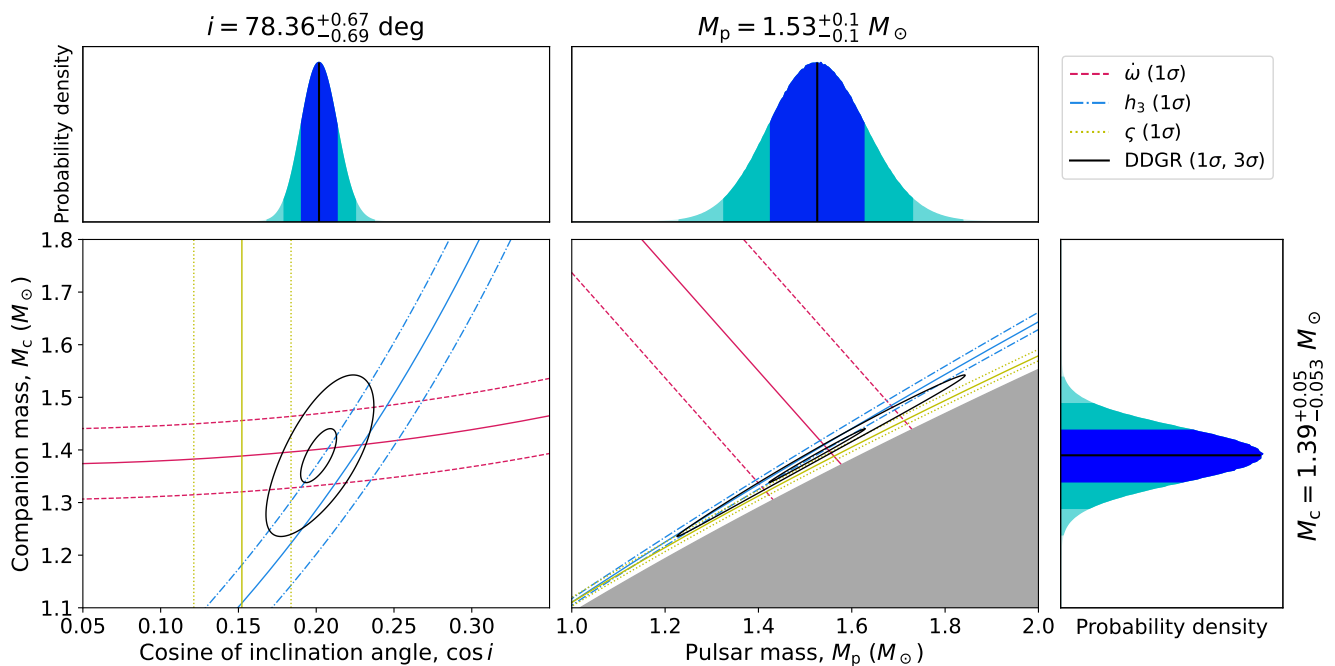


Fig. 5. Central plots: mass and inclination angle constraints from the DDH PK measurements and the χ^2 mapping with the DDGR model, both from the global fit and under the assumption of the Cs noise model (Table 2). The coloured solid lines represent the nominal values of the PK parameters, the coloured dashed lines their 1σ limits, and the solid black lines the 1σ and 3σ limits from DDGR. The shaded grey area in the right plot is the region excluded by the mass function ($i > 90$ deg). **Corner plots:** marginalised one-dimensional probability densities for M_p , M_c and $\cos i$ from DDGR χ^2 mapping, showcasing the median value (black solid line) and the 31.4%, 47.4% and 49.9% percentiles on both sides (shaded areas under the curve).

constraints on the $M_c - \cos i$ and $M_c - M_p$ spaces as derived both with the DDGR χ^2 mapping method and the constraints imposed by the independently measured $\dot{\omega}$, h_3 and ζ parameters, in both cases under the assumption of the Cs noise model. The resulting DDGR constraints are 1σ consistent with the measurement of $\dot{\omega}$ and h_3 , and 2σ consistent with ζ . This is also observed with the noise models **Ls**, **C**, **VC** and **VCS**. Only the assumption of the **L** noise model results in self-consistent constraints. The median values and the 68.2% percentiles of the marginal one-dimensional distributions for M_p , M_c and i are quoted as the measurements and their 1σ uncertainties in Table 3, where it is seen that all noise models present 1σ consistent constraints. We note that models with high-frequency cut-offs result in slightly lower mass ranges, going from $M_p = 1.59(10) M_\odot$ and $M_c = 1.42(5) M_\odot$ in **Ls** (Fig. A.1) to $M_p = 1.51(11) M_\odot$ and $M_c = 1.38(5) M_\odot$ in **VCS** (Fig. A.2). That is consistent with the variation of the h_3 values across noise models as exposed in Section 4.2, and shows how the DM noise is the main limiting factor in the precision of our mass measurements. On the other hand, the constraints on i are more sensitive to the inclusion or exclusion of red spin noise, with $i = 79.2(7)$ deg for the **L**, **C** and **VC** models and ranging from $i = 78.6(7)$ deg to $i = 78.2(7)$ deg from **Ls** to **VCS** models. Using extended uncertainty ranges from all the values listed in Table 3, we quote $M_t = 2.9 \pm 0.3 M_\odot$, $M_p = 1.54(15) M_\odot$, $M_c = 1.40(7) M_\odot$ and $i = 78.7 \pm 1.2$ deg, which constitute 10σ , 10σ , 20σ and 65σ constraints.

4.4. Discrepancies between PK parameters and GR

As shown in Fig. 5, ζ is only 2σ consistent with the DDGR constraints, and the h_3 and $\dot{\omega}$ parameters. To explore the cause of this slight discrepancy, we analyse the individual contribu-

tions to the PK parameters from segregated data sets. Keeping the noise models derived by TEMPO2/TempoNEST, we create two new isolated ToA time series: one with the ToAs derived from Parkes multibeam observations (multibeam), and another one with the ToAs derived from MeerKAT and the Parkes UWL observations (MeerKAT+UWL). These two sets differ significantly both in timing baseline and in ToA quality, with the Parkes multibeam-derived ToAs providing the longest baseline, but with the MeerKAT+UWL ToAs being much more precise and providing observing frequency information (Figs. 1 and 4). Subsequently, we repeat the TEMPO2 fits on each side.

The Shapiro delay measurement is not significantly affected by the split. In the multibeam fits, the orthometric Shapiro delay parameters are measured with larger uncertainties across all noise models ($h_3 = 4.1 - 4.7 \pm 2.1 \mu\text{s}$, $\zeta = 0.69 - 0.76 \pm 0.29$), but they are still consistent with the measurements from the global fit. On the other hand, the MeerKAT+UWL h_3 and ζ values listed in Table 6 are almost identical to the ones from the global fit quoted in Table 3. That is consistent with the Shapiro delay being primarily constrained by the MeerKAT ToAs owing to their higher precision (see Section 4.2).

The tension between the PK parameters is reduced in the MeerKAT+UWL fits. In the multibeam fits, the periastron advance $\dot{\omega}$ increases to $\dot{\omega} = 0.026(5) \text{ deg yr}^{-1}$, which is more than 1σ away from the global fit. Not only is this an unrealistic value, as it implies total system mass of $M_t = 5.5 \pm 1.7 M_\odot$, but it also suggests that the multibeam data set is somehow biased towards a larger $\dot{\omega}$ value. However, the MeerKAT+UWL fits give values much more consistent with the global fits, with $\dot{\omega} = 0.0163(14) \text{ deg yr}^{-1}$ from the extended uncertainties. The median value of $\dot{\omega}$ is slightly reduced within the 1σ uncertainties consistently across all noise models (Table 6) with only a small increase in uncertainty compared to the global fit ($\dot{\omega} =$

Table 4. Data reduction, model fit, spin, DM and astrometric parameters from the DDH TEMPO2/TempoNEST fits.

Data set	Global	multibeam	MeerKAT+UWL
Data reduction parameters			
Number of ToAs	1545	365	1180
First ToA (MJD)	55987.54	55987.54	58526.27
Last ToA (MJD)	60101.30	58581.61	60101.30
Solar System ephemeris	DE430	DE430	DE430
Timescale	TCB	TCB	TCB
Shortest correlated spin noise timescale, ν_{spin}^{-1} (days)	100	100	100
Shortest correlated DM noise timescale, ν_{DM}^{-1} (days)	50	50	50
Model fit parameters			
Log correlated spin noise amplitude, $\log A_{\text{spin}}$ (μs)	-11.7524	-12.0384	-11.8007
Log correlated DM noise amplitude, $\log A_{\text{DM}}$ (μs)	-10.0075	-11.7218	-9.993
Spin noise spectral index, γ_{spin} (μs)	1.49911	0.281109	1.0046
DM noise spectral index, γ_{DM} (μs)	1.57333	-1.80875	1.45055
Weighted root mean square of the timing residuals (μs)	6.995	23.571	6.094
Reduced χ^2	0.9650	1.0298	0.9643
Spin and astrometric parameters			
Reference epoch for spin, position and DM (MJD)	55991.22	55991.22	58526
Right ascension, RA (J2000, hh:mm:ss)	12:27:00.4414(4)	12:27:00.4412(4)	12:27:00.441(2)
Declination, DEC (J2000, dd:mm:ss)	-62:08:43.791(3)	-62:08:43.788(2)	-62:08:43.80(1)
Proper motion in RA (μ_{RA} , mas yr $^{-1}$)	-6.1(3)	-5.2(7)	-5.9 \pm 1.1
Proper motion in DEC (μ_{DEC} , mas yr $^{-1}$)	0.41 \pm 0.36	-0.4(7)	1.4 \pm 1.2
Spin frequency, F_0 (Hz)	28.962140551274(9)	28.96214055129(2)	28.96214051691(1)
Spin frequency derivative, F_1 (10^{-16} Hz s $^{-1}$)	-1.5677(4)	-1.570(2)	-1.5636(14)
Dispersion measure, DM_0 (pc cm $^{-3}$)	362.816(12)	362.808(11)	362.895(7)
First derivative of DM, DM_1 (10^{-2} pc cm $^{-3}$ yr $^{-1}$)	1.72(5)	2.8(9)	-1.86(9)
Second derivative of DM, DM_2 (10^{-3} pc cm $^{-3}$ yr $^{-2}$)	-2.3(9)	-3.1 \pm 2.1	3.1 \pm 2.1
Derived parameters			
Galactic longitude, l (deg)	300.082
Galactic latitude, b (deg)	0.591
Spin period, P_s (ms)	34.527834647774(10)	34.52783464775(2)	34.527834688742(19)
Spin period derivative, \dot{P}_s (10^{-19} s s $^{-1}$)	1.8690(5)	1.872(3)	1.8640(17)
NE2001 DM-derived distance, d (kpc)	8.3
YMW16 DM-derived distance, d (kpc)	8.5
Shklovskii contribution to \dot{P}_s (10^{-19} s s $^{-1}$)	\sim 0.26
Galactic potential contribution to \dot{P}_s (10^{-19} s s $^{-1}$)	\sim (-0.26)
Characteristic age, τ_c (Gyr)	2.9
Spin-down luminosity, $ \dot{E} $ (erg s $^{-1}$)	6.3×10^{32}
Surface magnetic field strength, B_{surf} (G)	2.6×10^9

Notes. The derived parameters are derived only for the global fit, the most constraining solution, and left blank for the multibeam and MeerKAT+UWL fit. The value of \dot{P}_s has not been corrected for the possible Shklovskii and Galactic potential contributions.

0.0171(11) deg yr $^{-1}$, Table 3). With this subtle change, $\dot{\omega}$, h_3 and ζ become 1σ consistent with each other across all noise models.

In an attempt to understand the origin of the apparent biases introduced by the the multibeam data set, we have performed two extra TEMPO2/TempoNEST runs with $\nu_{\text{spin}}^{-1} = 100$ days and $\nu_{\text{DM}}^{-1} = 50$ days on the multibeam and MeerKAT+UWL data sets, and compared the resulting noise and timing parameters with those of the Cs model derived in the global fit (Table 2). Table 4 and 5 show the global fit, the multibeam fit and the MeerKAT+UWL fit results side to side. In Table 4, it becomes readily evident that TEMPO2/TempoNEST converges on similar timing noise models for the global and MeerKAT+UWL data sets. Table 5 also shows that the MeerKAT+UWL PK parameter

measurements are also virtually identical to those derived with the assumption of the Cs model, presented in Table 6. However, the noise model diverges in the isolated multibeam data set and it is unable to converge on realistic values, showing that the Parkes multibeam data does not have enough timing precision and bandwidth to constrain the spin and DM timing noise. This could explain why the multibeam gives a discrepant $\dot{\omega}$ measurement, and why it could be biasing the global fit measurements as well.

In light of this, we repeat the χ^2 mapping of DDGR solutions with the MeerKAT+UWL data set only and with the assumption of the noise models derived in the global TEMPO2/TempoNEST fits (Table 2), deriving the M_p , M_c and i constraints quoted in Table 6. Similar to the global fits, $\dot{\omega}$ and h_3 dominate the con-

Table 5. Orbital Keplerian and PK parameters from the DDH TEMPO2/TempoNEST fits, and mass constraints from the DDGR χ^2 mapping fits.

Data set	Global	multibeam	MeerKAT+UWL
Keplerian orbital parameters			
Orbital period, P_b (days)	6.7210192(3)	6.72102(2)	6.7210189(4)
Orbital eccentricity, e	0.00114918(4)	0.0011492(4)	0.00114918(5)
Longitude of periastron, ω (deg)	27.090(9)	27.07(3)	27.211(12)
Projected semi-major axis of the pulsar orbit, x (ls)	23.200666(3)	23.20066(3)	23.200665(3)
Epoch of periastron, T_0 (MJD)	55991.6995(2)	55991.6991(6)	58525.52384(9)
Post-Keplerian (PK) orbital parameters			
Rate of periastron advance $\dot{\omega}$ (deg yr $^{-1}$)	0.01710(83)	0.0252(48)	0.0163(11)
Orthometric amplitude of Shapiro delay, h_3 (μ s)	3.45(23)	3.5 ± 1.8	3.44(23)
Orthometric ratio of Shapiro delay, ζ	0.858(27)	0.76(27)	0.853(30)
Derivative of orbital period, \dot{P}_b (10^{-13} s s $^{-1}$)	3.7 ± 2.5	-10 ± 30	8 ± 40
Estimated Shklovskii contribution to \dot{P}_b (10^{-13} s s $^{-1}$)	~ 4.5
Estimated Galactic potential contribution to \dot{P}_b (10^{-13} s s $^{-1}$)	$\sim (-4.5)$
Derivative of projected semi-major axis, \dot{x} (10^{-15} ls s $^{-1}$)	-9.1 ± 7.2	-88 ± 42	-17 ± 11
Estimated maximum proper motion contribution to \dot{x} , $ \dot{x}_{\max} $ (10^{-15} ls s $^{-1}$)	~ 4.2
Mass and orbital geometry constraints			
Mass function, f_M (M_\odot)	0.297	0.297	0.297
Total mass, M_t (M_\odot)	$3.1^{+0.6}_{-0.8}$	5.5 ± 1.7	$3.0^{+0.7}_{-1.0}$
Companion mass, M_c (M_\odot)	1.39(5)	...	1.31(7)
Pulsar mass, M_p (M_\odot)	1.53(10)	...	1.37(14)
Inclination angle, i (deg)	78.4(7)	...	78.9(8)
Longitude of ascending node, Ω_a (deg)	$86/266^{+76}_{-78}$

Notes. The non-GR contributions to \dot{P}_b and \dot{x} are derived only from the global fit constraints, where the proper motion measurement is the most significant (Table 4). Mass and orbital geometry constraints are derived from the χ^2 mapping of DDGR solutions, as exposed in Sections 4.3, 4.4 and 4.5.

Table 6. Constraints on the PK parameters and the component masses from the MeerKAT+UWL fits.

Model	$\dot{\omega}$ (deg yr $^{-1}$)	h_3 (μ s)	ζ	M_p (M_\odot)	M_c (M_\odot)	i (deg)
L	0.0163(12)	3.9(3)	0.82(4)	1.42(14)	1.33(7)	79.6(8)
Ls	0.0166(11)	3.7(3)	0.84(3)	1.43(14)	1.34(7)	79.2(8)
C	0.0163(12)	3.7(3)	0.84(4)	1.39(15)	1.32(7)	79.4(8)
Cs	0.0164(11)	3.4(3)	0.86(3)	1.37(14)	1.31(7)	78.9(8)
VC	0.0162(12)	3.7(3)	0.84(4)	1.38(15)	1.32(8)	79.4(9)
VCs	0.0160(11)	3.4(2)	0.85(3)	1.31(13)	1.28(7)	78.9(8)
extended	0.0163(14)	3.7(5)	0.84(6)	1.36(20)	1.31(10)	79.2 ± 1.1

Notes. The PK parameters were measured in the MeerKAT+UWL fit with TEMPO2 under the assumption of the noise models as derived by TEMPO2/TempoNEST (Table 2). The component masses were derived from the χ^2 mapping of DDGR solutions (Section 4.4). The **extended** row shows comprehensive uncertainties accounting for all measurements across the different noise models.

straints, but this time, the DDGR limits are 1σ consistent with all of the PK parameters. Like in the global fits, the more constraining noise models result in lower mass ranges, ranging from $M_p = 1.31(31) M_\odot$ and $M_c = 1.28(7) M_\odot$ with the **VCs** noise model (Fig. A.3) to $M_p = 1.43(14) M_\odot$ and $M_c = 1.34(7) M_\odot$ with the **Ls** noise model (Fig. A.4). For reference, Fig. A.5 in the Appendix (7) shows the counterpart for Fig. 5, with the assumption of the **Cs** noise model on the MeerKAT+UWL data set. Nonetheless, the uncertainty ranges are still 1σ consistent with the global fits presented in Table 3. Accounting for extended uncertainties from all measurements in Table 6, we quote

$M_t = 2.7 \pm 0.4 M_\odot$, $M_p = 1.36(21) M_\odot$, $M_c = 1.30(9) M_\odot$ and $i = 79.3 \pm 1.1$ deg from the MeerKAT+UWL global fits, which are 7σ , 6σ , 14σ and 77σ measurements and are in 1σ consistency with the ones quoted in Section 4.3.

Finally, we attest that \dot{P}_b and \dot{x} can only be constrained in the global fit. Both the multibeam and the MeerKAT+UWL fits are unable to constrain to \dot{P}_b and \dot{x} . As shown in Table 5, the uncertainties on both parameters increase by an order of magnitude. Therefore, it is evident that only the accumulated baseline of the global fit can constrain them.

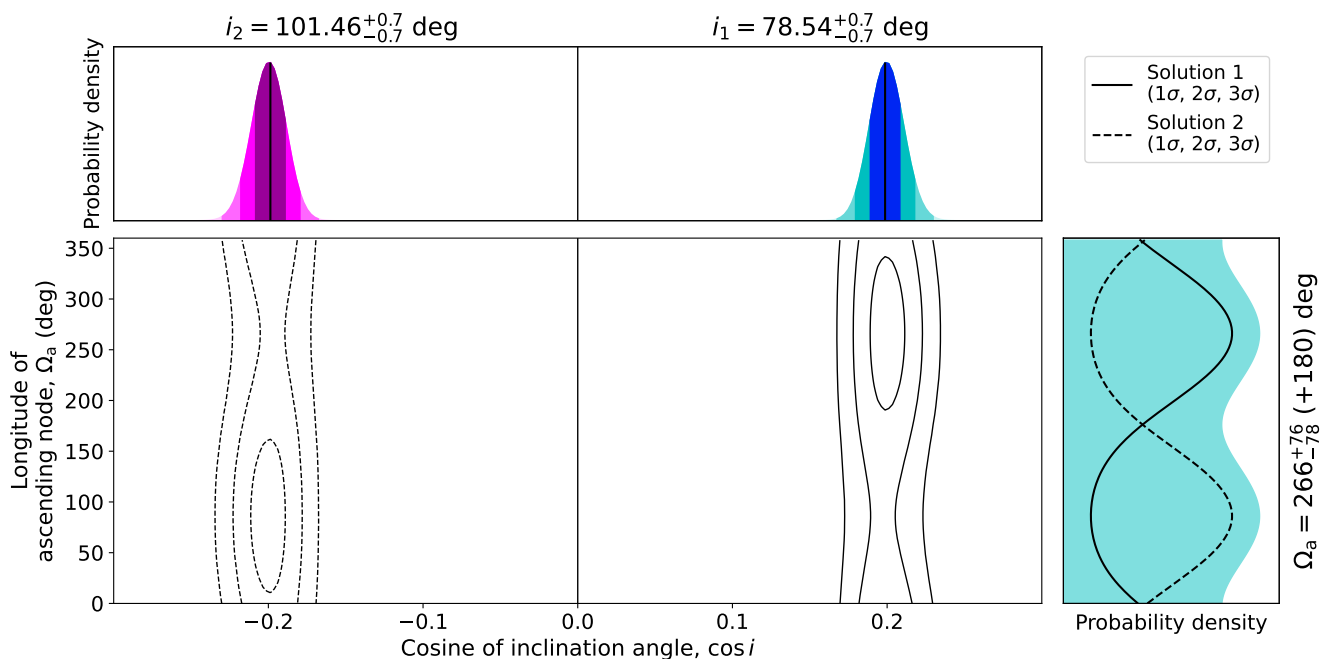


Fig. 6. Central plots: constraints on the $\Omega_a - \cos i$ space derived from the χ^2 mapping of DDGR solutions enforcing consistency with eq. (11) in the global fit and assuming the Cs noise model (table 2). The solid contours represent the explored space ($\cos i > 0$), while the dashed contours are derived from symmetries in eq. (11). **Corner plots:** marginalised one-dimensional probability densities for $\cos i$ and Ω_a , showcasing the median value (black solid line) and the 31.4%, 47.4% and 49.9% percentiles on both sides (shaded areas under the curve).

4.5. Orbital geometry constraints

In Section 4.2 it was noted that the uncertainty in the constraints of \dot{x} across have a similar size as the $|\dot{x}_{\max}| \approx 4.2 \times 10^{-15}$ expected from the proper motion, as quoted in Table 5. Therefore, we investigate how the DDGR solutions are affected upon enforcement of consistency between \dot{x} , μ and the orbital geometry of the system. Assuming the noise models derived with TEMPO2/TempoNEST, we implement the same likelihood approach from Section 4.3 with two major modifications. First, the mapping is now done in a uniform three-dimensional grid on the $M_t - \cos i - \Omega_a$ space. Second, equation (11) is implemented by forcing the excess \dot{x} value to be consistent with the i , Ω_a and $\mu = (\mu_{\text{RA}}, \mu_{\text{DEC}})$ values. To compensate for the extra dimensionality, the grid resolution is reduced to avoid a manifold increase of the computational running time of this experiment, with only 64 points along the M_t axis across 10σ , 60 points along the $\cos i$ across 12σ and 180 points across the $0 \leq \Omega_a < 360$ range. In addition, equation (11) is symmetric with respect to the transformation $i \rightarrow 180 \text{ deg} - i$ and $\Omega_a \rightarrow \Omega_a + 180 \text{ deg}$. Therefore, the $\cos i < 0$ side of the explored space is derived by implementing this transformation. This last point is true only because the distance to J1227–6208 is large enough so that the orbital motion of Earth does not introduce year-long periodic contributions to \dot{x} . Finally, we integrate the likelihood distribution along the M_t axis to derive two-dimensional likelihood distribution on the $\Omega_a - \cos i$ space, from which the marginal probability distributions for Ω_a and $\cos i$ are derived.

The constraints on $\cos i$ and Ω_a are drawn on Fig. 6. As expected, the constraints on i are consistent with those derived in Section 4.3. The value of Ω_a is not constrained owing to the large overlap of the $\cos i > 0$ and $\cos i < 0$ probability distributions, but the probability density contours show that two regions in the $\cos i - \Omega_a$ are preferred. For $\cos i > 0$, the longitude of ascending node is constrained at $\Omega_a = 266 \pm 78 \text{ deg}$, while for $\cos i < 0$ it is

constrained at $\Omega_a = 86 \pm 78 \text{ deg}$. From equation 11, using the values of x , i , μ_{RA} and μ_{DEC} presented in Table 4 and $\Omega_a = 266 \text{ deg}$, we predict a value of $\dot{x} \approx -4.2 \times 10^{-15} \text{ ls s}^{-1}$, in full consistency with the values presented in Table 3. Therefore, it is clear that the measured excess \dot{x} originates from the proper motion of the system in the sky.

4.6. Spin and orbital period evolution constraints

As shown in Table 4, in the global fit we measure the spin evolution parameters P_s and \dot{P}_s with high significance, showing that J1227–6208 is indeed a mildly recycled pulsar. However, the Shklovskii effect and Galactic potential field affect \dot{P}_s in the same way as they affect \dot{P}_b , following equation (10). The estimated values of these contributions are listed at the end of Table 4, making it evident that albeit they are smaller than the measurement ($\sim 10^{-20} \text{ s s}^{-1}$ against $\dot{P}_s = 1.8690(5) \times 10^{-19} \text{ s s}^{-1}$), they can nonetheless be significant. Thus, we should be cautious of pulsar parameters derived from P_s and \dot{P}_s . Since a parallax distance measurement is out of the question, the best prospect for constraining the true combined contribution of the Shklovskii effect and Galactic potential field is to improve the \dot{P}_b measurement, on which these effects are orders of magnitude larger than the GR prediction. Therefore, a measurement of \dot{P}_b will be direct measurement of the Doppler factor derivative. Nonetheless, with the current observations, the consistently positive sign of \dot{P}_b across all noise models (Table 3) already suggests a dominance of the Shklovskii effect over the Galactic potential contribution.

5. Astrophysical Implications

5.1. J1227–6208 as a DNS system

The mass ranges derived in Sections 4.3 and 4.4 and presented in Tables 3 and 6 are consistent with the mass distribution of the

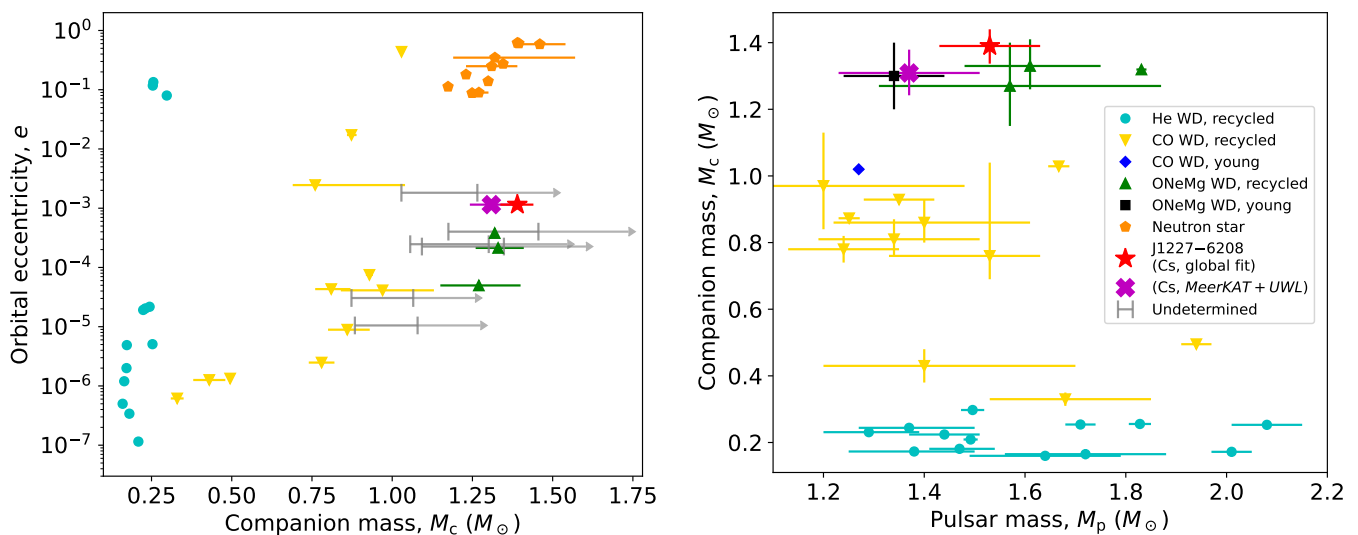


Fig. 7. Left: orbital eccentricity against companion mass from recycled binary pulsars in the Galactic field with companion mass constraints, distinguished by the nature of their companions. For systems without timing mass measurements ("Undetermined" in the legend), the lower constraints on the minimum and median M_c values derived from the mass function ($i = 90, 60$ deg) are plotted. **Right:** companion mass against pulsar mass for all PSR–WD systems with mass measurements from timing in the Galactic field. The constraints on J1227–6208 constraints plotted twice, from the global fit (red star) and the MeerKAT+UWL fit (magenta star). In both cases, we use the Cs noise model results. Constraints on systems besides J1227–6208 are taken from https://www3.mpifr-bonn.mpg.de/staff/pfreire/NS_masses.html and references therein, and from Camilo et al. (2001) (PSR J1435–6100), Cruces et al. (2021) (PSR J2338+4818), Edwards & Bailes (2001) (PSR J1157–5112), Gautam et al. (2022) (PSR J1952+2630), Jang et al., in prep. (PSR J1439–5501), Martinez et al. (2019) (PSR J0709+0458), Parent et al. (2019) (PSR J1932+1756) and Tan et al. (2020) (PSR J1658+3630).

double-NS (DNS) population, with M_c being significantly above the current lower mass limit of a NS ($1.17 M_\odot$, Martinez et al. 2015), making a NS nature a hypothesis in need of consideration.

Recycled pulsars with massive WD and NS companions follow a similar evolutionary path. With original companions more massive than $5 M_\odot$ (Lazarus et al. 2014), these systems go through an intermediate-mass or high-mass X-ray binary (IMXB or HMXB) stage, resulting in a dynamically unstable mass transfer and the formation of a common envelope (CE, e.g. van den Heuvel 2019). After the hydrogen-rich CE is expelled, the system becomes a circular PSR–He naked star. Stable mass accretion on to the NS occurs when the companion leaves the He main sequence and the system enters a short-lived (less than 100 kyr) Case BB RLO stage, leading to the partial recycling of the pulsar (Lazarus et al. 2014). Afterwards, and if the stripped He star has retained enough mass ($\geq 1.45 M_\odot$), the companion will undergo an electron-capture supernova, forming a second NS (Tauris et al. 2015, 2017). This process entails the loss $0.2 - 0.4 M_\odot$ and a supernova kick of $< 50 \text{ km s}^{-1}$ that either disrupts the system or introduces a significant orbital eccentricity ($e \geq 0.1$, Tauris et al. 2017). On the other hand, if the stripped companion is unable to trigger a supernova, it becomes a massive WD instead (Lazarus et al. 2014; Tauris et al. 2012).

We argue that J1227–6208 is very unlikely to be a DNS system based on its orbital eccentricity. The left plot of Fig. 7 depicts the orbital eccentricity e of recycled pulsars against M_c and it shows that, while the M_p in J1227–6208 is consistent with the DNS population, its e value is two orders of magnitude below those of known DNS systems. Instead, it lays among other massive recycled PSR–CO/ONeMg WD systems. While Tauris et al. (2017) show that very low eccentricities ($e < 0.01$) in DNS are technically possible, they also argue that this scenario is extremely unlikely, requiring an extraordinary fine-tuning of the supernova kick magnitude and direction. That is strong evi-

dence against the companion of J1227–5936 having undergone a supernova, making it a massive WD instead.

5.2. J1227–6208 as a massive PSR–WD system

J1227–6208 thus belongs to an emerging class of massive recycled PSR–ONeMg WD systems. The right side of Fig. 7 maps measured PSR–WD component masses in a $M_c - M_p$ diagram, showing that J1227–6208 lies among the well-studied massive systems PSR J2222–0137, PSR J1528–3146 and J1439–5501, represented by the green triangles. J1227–6208 also shares with these three systems similar spin properties ($P_0 = 34.52$ ms against 32.82, 60.82 and 28.64 ms), binary period ($P_b = 6.72$ days against 2.45, 3.18, and 2.12 days) and orbital eccentricity ($e = 1.15 \times 10^{-3}$ against 4.65×10^{-4} , 2.13×10^{-4} and 4.99×10^{-5}), suggesting a similar nature. Therefore, it is very plausible that J1227–6208 has followed the evolutionary path of recycled PSR–ONeMg WD systems ($M_c \geq 1.1 M_\odot$). It should be noted that the young system PSR B2303+46, shown as a black square in Figs. 7, is the result of an exotic evolution where the WD formed before the pulsar and thus no recycling has occurred in it (van Kerkwijk & Kulkarni 1999; Tauris & Sennels 2000).

As we argue in favour of a WD nature for the companion, the possibility of M_c laying beyond the Chandrasekhar limit (Section 4.3) is brought into question. Theoretical models predict that fast-rotating WDs may exist in the $1.38 < M_{\text{WD}}/M_\odot < 1.48$ mass range without collapsing in a supernova (e.g. Yoon & Langer 2005). However, these conditions can only be the result of accretion and the spin-up in the WD, or be the product of a WD merger. Both of these scenarios are difficult to reconcile with the evolutionary model proposed above and the low orbital eccentricity, and therefore the mass of the companion of J1227–6208 is likely lower than $1.38 M_\odot$. Continued timing in the future will

be essential to increase the precision of the mass constraints so that a more definitive statement can be made on this aspect.

J1227–6208 and its companion are the fourth partially recycled pulsar with a $M_c > 1.1 M_\odot$ ONeMg WD companion with mass measurements from timing. As seen on the right plot of Fig. 7, it is tempting to see this population as an emerging class distinct from partially recycled pulsars with the massive CO WD companions, in addition to the already-known separation between massive CO WD systems ($M_c \gtrsim 0.7 M_\odot$) and the fully recycled millisecond pulsars with light He and CO WD companions ($M_c \lesssim 0.5 M_\odot$) McKee et al. (2020); Shamohammadi et al. (2023). However, a gap between CO WD and ONeMg WD masses is not predicted by theory. Furthermore, the left plot of Fig. 7 shows that a handful of known massive systems without mass measurements can potentially fill this gap: PSR J1435–6100 (Camilo et al. 2001), PSR J2338+4818 (Cruces et al. 2021), PSR J1157–5112 (Edwards & Bailes 2001), PSR J1952+2630 (Jang et al., in prep.), PSR J0709+0458 (Martinez et al. 2019), PSR J1932+1756 (Parent et al. 2019) and PSR J1658+3630 (Tan et al. 2020). Thus, this gap could be spurious, arising from the reduced size of the sample of mass measurements in massive systems. New mass measurements and the discovery and follow-up of further massive partially recycled PSR–ONeMg WD systems will be key in confirming whether the white dwarf mass distribution is trimodal or if this notion is just a statistical fluke.

5.3. The pulsar mass of J1227–6208

Theoretical models for recycled pulsars with the most massive WD companions suggest that these systems went through a short phase of accretion during post-CE Case BB RLO from their naked He-star companion, resulting in observed spin-up periods of $P_s \gtrsim 20$ ms. According to Tauris et al. (2012), the amount of mass accreted by a recycled pulsar given a P_s can be estimated with the following equation:

$$\Delta M_p \approx 0.22 M_\odot \frac{(M_p/M_\odot)^{1/3}}{(P_s/\text{ms})^{4/3}}. \quad (12)$$

Assuming its current spin period of $P_s \approx 34.5$ ms results in the accretion of $0.0022 M_\odot$ from its companion during recycling. On the other hand, assuming a possible initial spin-up period of $P_s \approx 20$ ms results in the accretion of at most $0.0045 M_\odot$ from its companion. In both cases, the implication is that the current M_p measurement is close its birth mass. Therefore a more precise measurement of M_p will contribute to the statistics of NS birth masses, like in the similar systems PSR J2222–0137, PSR J1534–3146 and PSR J1439–5501. In fact, the measurement of $M_p = 1.76(6) M_\odot$ PSR J2222–0137 in Cognard et al. (2017) ($M_p = 1.831(10) M_\odot$ in Guo et al. 2021) has already expanded such distribution on its upper end.

If the amount of accreted matter estimated from theory is correct, the mass-transfer rate was likely Eddington or super-Eddington. For a NS of $1.5 M_\odot$, the Eddington luminosity limit is $L \approx 1.5 \times 10^{38} \text{ erg s}^{-1}$ and the accretion-to-luminosity efficiency is $L \approx 0.1 \times \dot{M} c^2$ (Shakura & Sunyaev 1973; Poutanen et al. 2007), resulting in a maximum accretion rate of $\dot{M} \approx 0.03 M_\odot \text{ Myr}^{-1}$. Simulations find that the duration of the accretion stage during the Case BB RLO is $\leq 100,000$ yr for massive PSR–WD systems (Lazarus et al. 2014; Tauris et al. 2015, e.g.), and Cognard et al. (2017) even found that the accretion time was $\leq 20,000$ yr for the massive PSR–ONeMg WD system in PSR J2222–0137. The Eddington limit would allow for the accretion

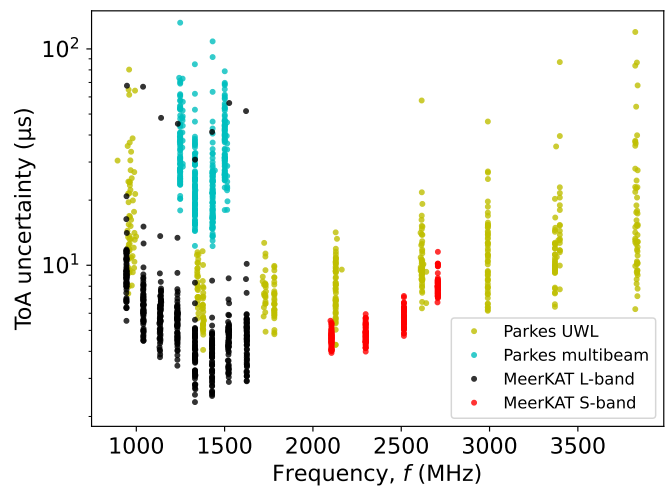


Fig. 8. ToA uncertainty against observing frequency for each telescope receiver. The highest and lowest frequencies of the Parkes multibeam and MeerKAT S-band data sets are biased upwards because the signal drops off at the edge of the bands (see Fig. 1).

of at most $0.003 M_\odot$ in the span of 100,000 yr, and $5 \times 10^{-4} M_\odot$ in 20,000 yr, implying that if the recycling process occurred on a similar time span for J1227–6208, then it has accreted either close to the Eddington limit or significantly above it like in PSR J2222–0137. This is a plausible scenario, as super-Eddington accretion onto NSs has been directly observed in extra-galactic ultra-luminous X-ray sources such as NGC 5907 X-1 (Israel et al. 2017), NGC 300 ULX1 (Carpano et al. 2018) and M82 X-2 (Bachetti et al. 2014). However, an alternative explanation is that the spin-up efficiency is larger than what is predicted by Tauris et al. (2012), requiring less mass accretion to reach a similar P_s .

6. Future prospects

6.1. Prospects for timing

Future timing observations of J1227–6208 should seek to strike a balance between its steep spectrum and the ISM-induced effects. Fig. 8 portrays how ToA uncertainty evolves with f across different receivers, and it shows that scattering affects the ToA quality negatively at $f < 1,300$ MHz, leading to an increase of timing uncertainty. The best ToA quality is found at the $f = 1.3\text{--}2.2$ GHz range, while at $f > 2,200$ MHz the steep spectrum starts hampering the S/N , leading to another increase in timing uncertainty. Another factor to take into account is that, as reported in Section 4.1, red DM noise is very prominent, making it preferable to observe at high frequencies where its amplitude is lower. However, doing so comes at the price of achieving a sub-optimal S/N and ToA quality due to the steep spectral index reported in Section 3. Therefore, MeerKAT observations with the S-band receivers at the S0 configuration (1750–2625 MHz) will offer the best compromise between a high ToA precision and a reduced ISM influence, with $A_{\text{DM},1700} = 0.68 \times A_{\text{DM}}$ and $A_{\text{DM},2600} = 0.28 \times A_{\text{DM}}$, thus enabling a precision increase on the measurement of PK parameters. In complement to this, UWL observations will be essential to track the DM evolution to properly model the still-present DN noise in the MeerKAT S-band ToAs.

The significance of the PK parameters will improve with an increasing baseline. The most significant improvement in the

mass constraints will come from an improved measurement of $\dot{\omega}$. Assuming that the uncertainty on $\dot{\omega}$ scales with the timing baseline according to the power law (Damour & Taylor 1992)

$$\Delta\dot{\omega}' \approx \Delta\dot{\omega} \times \left(\frac{T}{4.31 \text{ yr}} \right)^{-3/2}, \quad (13)$$

where 4.31 yr is the timing baseline of the MeerKAT+UWL data set, we expect $\Delta\dot{\omega}' \approx \Delta\dot{\omega}/2$ with just two extra years of timing. This improvement will reduce the total mass measurement uncertainty by 65% if we assume the current MeerKAT ToA uncertainty, aiding a more robust settlement or confirmation of any discrepancies between the PK parameters in the global fit.

Tighter constraints on \dot{P}_b and \dot{x} will also lead to an independent estimate of the distance of J1227–6208 and a better constraint on its orbital geometry. However, since these measurements are dependent on the global 11.26 year baseline, reducing uncertainty will require more time. Assuming once again a power law evolution of the uncertainties \dot{P}_b (Damour & Taylor 1992)

$$\Delta\dot{P}_b' \approx \Delta\dot{P}_b \times \left(\frac{T}{11.26 \text{ yr}} \right)^{-5/2}, \quad (14)$$

then another decade of timing will be required to achieve a 3σ detection of \dot{P}_b . Constraints on the orbital geometry will also require an improvement of the measurement of the proper motion. Following the power law evolution of the uncertainty on \dot{x} (Damour & Taylor 1992)

$$\Delta\dot{x}' \approx \Delta\dot{x} \times \left(\frac{T}{11.26 \text{ yr}} \right)^{-3/2}, \quad (15)$$

two more decades of timing will be necessary to achieve a 3σ detection on \dot{x} . However, as seen in Section 4.5, constraints on the $\Omega_a - \cos i$ can already be achieved even with a low-significance detection. Furthermore, the proper motion vector measurement will continue to improve alongside it, leading to more significant constraints in the $\Omega_a - \cos i$ space before that time.

6.2. Prospects for an optical detection

There would be obvious benefits to having an optical detection of the companion of J1227–6208. Besides the confirmation of its WD nature, a measurement of its colour index and magnitude could be used to constrain its age with the help of WD evolutionary models. This would provide an independent measurement of the mass and age of the companion of J1227–6208 like other massive PSR–WD systems, such as PSR J1528–3146 (Jacoby et al. 2006) and PSR J1439–5501 (Pallanca et al. 2013). That would allow, for example, for a true estimate the initial spin-up period.

As of now, we are unable to report an optical detection. *Gaia* DR3 is sensitive to sources with magnitude $G \approx 20.7$ (Gaia Collaboration et al. 2016, 2023). Assuming the YMW16-derived DM distance of $d = 8.5 \text{ kpc}$, detection would require an absolute magnitude of at most $M_G \approx 6$ to be detected, too bright for any WD. The closest reported *Gaia* DR3 source⁹ is 0.29 arcsec away from the timing position, with a color index $B - R = 1.59$ and magnitude $G = 17.4$. Its parallax distance is $d = 5.3 \pm 2.0$, giving it an absolute magnitude of $M_G = 3 - 5$, and putting it either on the main sequence or the giant branch. Therefore, this source is most likely not associated with J1227–6208.

⁹ Designation: *Gaia* DR3 6054663745667894016

A potential detection will be possible only with the most powerful optical and infrared telescopes available. Assuming $d = 8.5 \text{ kpc}$, we use the cooling tracks provided by Bergeron et al. (2011)¹⁰ for a $M_{\text{WD}} = 1.3 M_{\odot}$ with a He atmosphere to predict visible and infrared magnitudes given an age. If the age of the system is consistent with the characteristic age of $\tau_c = 2.93 \text{ Gyr}$, then the companion will have a optical, red and infrared magnitudes of $V, R, I > 30$ and it will be undetectable. But if, like in PSR J1439–5501, the true age is significantly younger than τ_c for instance only 100 Myr old (Pallanca et al. 2013), the magnitudes could reach $V, R, I < 27$, making it potentially detectable in long exposure by sensitive optical and infrared telescopes such as the Very Large Telescope, the *Hubble* Space Telescope or the *James Webb* Space Telescope.

7. Conclusions

This study adds J1227–6208 to the rare class of confirmed mildly recycled pulsars with massive ONeMg WD companions ($M_{\text{WD}} > 1.1 M_{\odot}$), along with PSR J2222–0137, PSR J1528–3146 and PSR J1439–5501. In addition, we have provided a detailed study of the pulsar’s emission and the origin of the PK parameters measured in pulsar timing. The study includes 33 hours of Parkes multibeam data since 2012, 72 hours of Parkes ULW data since 2020, 25 hours of MeerKAT data since 2019 and 19 hours of MeerKAT S-band data from 2023, producing a timing baseline of more than 11 years.

Taking advantage of the large frequency coverage offered by these receivers to study the profile evolution of J1227–6208, we measure a steep flux density spectral index of $2.06 < \alpha < 2.35$ and a flat scattering index $3.33 < \beta < 3.62$, with a scattering timescale of $\tau_s \approx 1.2 \text{ ms}$ and a mean flux density of $F_m = 530 - 620 \text{ } \mu\text{Jy}$ at the reference frequency of 1 GHz. Due to the combined effect of scattering and spectral properties, the largest peak flux density is observed at the frequency of 1.2 – 1.3 GHz, with $F_{\text{max}} = 13 - 14 \text{ mJy}$. Around 15% of the emission of J1227–6208 is linearly polarised, with a behaviour that does not resemble the rotating vector model, and a further ~15% of the emission is circularly polarized.

The timing of J1227–6208 suffers from red spin noise and, more prominently, red DM noise. We have implemented a Bayesian nested sampling algorithm to measure the parameters of the DDH timing model, including the spectral modelling of red DM, red spin noise and white noise, and the timing model parameters. We derived six different noise models: three with correlated spin noise and three without it, using different frequency cut-offs in all cases. We find that the red DM noise amplitude at 1400 MHz is almost two orders of magnitude larger than the red spin noise amplitude, and that models with both correlated spin and correlated DM noise with high-frequency cut-offs are favoured by the sampling evidence. Nonetheless, all of the resulting PK parameters are consistent across models within 1σ uncertainty. The Shapiro delay orthometric parameters, h_3 and ζ , and the periastron advance $\dot{\omega}$ are dominated by the MeerKAT-derived ToAs, while the constraints of the orbital period derivative \dot{P}_b and the projected semi-major axis derivative \dot{x} are possible only with the accumulated timing baseline.

We argue that the constraints on \dot{P}_b and \dot{x} are physical despite their low significance. \dot{P}_b presents a consistent sign across all noise models and is about the same order of magnitude as the combined prediction of the Shklovskii effect given by the DM

¹⁰ Tables available here: <https://www.astro.umontreal.ca/~bergeron/CoolingModels/>

distance and the proper motion vector and the Galactic acceleration fields ($\dot{P}_b \sim 10^{-13} \text{ s s}^{-1}$), therefore implying that a more significant detection will occur in the following years. This detection will also clarify the magnitude of the Shklovskii effect and the Galactic acceleration on the spin period derivative \dot{P}_s . The situation is similar for \dot{x} , as we predict $|\dot{x}_{\text{max}}| \approx 4.2 \times 10^{-15} \text{ ls s}^{-1}$ for from the proper motion vector, $i = 79$ deg and a favourable longitude of ascending node angle Ω_a , which is of the same order of magnitude as the timing constraints. The mapping of solutions that implement consistency with the excess \dot{x} , the proper motion, i and Ω_a indicate that the resulting χ^2 is indeed sensitive to the location in the $\Omega_a - \cos i$ grid, with a preference for either $\Omega_a = 266 \pm 78$ deg and $i = 79$ deg, or $\Omega_a = 86 \pm 78$ deg and $i = 101$ deg. This parameter is also likely to get a more significant detection in the following years.

With the noise models from the DDH fits, we measure the pulsar mass M_p , companion mass M_c and inclination angle i by performing a mapping of solutions under the assumption of GR across all noise models, and attest that they are consistent with the PK parameters. In the global fit, the $h_3 = 3.6 \pm 0.5 \mu\text{s}$ and $\dot{\omega} = 0.0171(11) \text{ deg yr}^{-1}$ measurements are 1σ consistent with the assumption of GR, while $\zeta = 0.85 \pm 0.05$ is 2σ consistent with GR, resulting in $M_p = 1.54(15) M_\odot$, $M_c = 1.40(7) M_\odot$ and $i = 78.7 \pm 1.2$ deg in a conservative uncertainty range that includes all noise models. However, if we exclude the Parkes multibeam observations from the analysis, the median of the periastron advance is reduced to $\dot{\omega} = 0.0163(14) \text{ deg yr}^{-1}$, resulting in 1σ consistency between the three PK parameters and GR, and the mass constraints of $M_p = 1.36(20) M_\odot$, $M_c = 1.31(10) M_\odot$ and $i = 79.2 \pm 1.1$ deg. All of these measurements are within 1σ uncertainty overlap, and they result in the total ranges of possible values of $2.3 < M_t/M_\odot < 3.2$, $1.16 < M_p/M_\odot < 1.69$, $1.21 < M_c/M_\odot < 1.47 M_\odot$ and $75.5 < i/\text{deg} < 80.3$. This wide range of possible values demonstrates that DM variability and its modelling as red DM noise is the main limiting factor of the precision of our timing analysis.

Despite the companion mass uncertainty range extending into the regime of known NS masses, the probability of it being a NS is extremely low due to the very small orbital eccentricity ($e = 1.15 \times 10^{-3}$), which is much more consistent with the massive recycled PSR–CO/ONeMg WD population. The WD mass measured in this work is significant as it overlaps with the companion masses measured for three other similar systems. This measurement explores the potential multi-modality of the WD mass distribution noted in previous works, which suggests that the WD mass distribution is not continuous, but characterised by discrete clumps. Whether WDs with $M_{\text{WD}} \gtrsim 1.1 M_\odot$ are segregated from their $0.7 \lesssim M/M_\odot \lesssim 1.0$ counterparts or not will be decided by further measurements of systems in these mass ranges. Regarding the pulsar mass, given the relatively large spin period of 34 ms, J1227–6208 has likely accreted no more than $0.0045 M_\odot$ during the recycling process, that a precise measurement of M_p will contribute to the NS birth mass distribution. However, if accretion occurred in a time period significantly shorter than 100,000 years like in the case of PSR J2222–0137 (Cognard et al. 2017), this would imply either super-Eddington accretion or a larger spin-up efficiency than predicted in Tauris et al. (2012).

Future timing of this system will be key for constraining the PK parameters and the mass constraints even further. The most precise ToAs are produced in the 1.3 – 2.2 GHz frequency range due to the balance between the steep spectral index and scattering. However, the presence of red DM noise requires that future observations are taken at higher frequencies, making the

1.7 – 2.6 GHz MeerKAT S-band receiver on the S0 configuration the best observing band in the future. Optical detection of the WD companion may be possible in long exposures with the most powerful optical/infrared telescopes if the system is younger than a few hundred Myr, leading to an independent confirmation of the nature of the system, or otherwise to a lower limits of its true age.

Acknowledgements. The MeerKAT telescope is operated by the South African Radio Astronomy Observatory (SARAO), which is a facility of the National Research Foundation, an agency of the Department of Science and Innovation. SARAO acknowledges the ongoing advice and calibration of GPS systems by the National Metrology Institute of South Africa (NMISA) and the time space reference systems department of the Paris Observatory. The Parkes radio telescope is part of the Australia Telescope National Facility (ATNF), which is funded by the Australian Government for operation as a National Facility managed by the Commonwealth Scientific and Industrial Research Organisation (CSIRO). We acknowledge the Wiradjuri people as the Traditional Owners of the Observatory site. This work used the OzSTAR national facility at Swinburne University of Technology. OzSTAR is funded by Swinburne University of Technology and the National Collaborative Research Infrastructure Strategy (NCRIS). All authors affiliated with the Max Planck Institute for radioastronomy (MPIFR) acknowledge the continuing valuable support from the Max-Planck Society (MPG). Vivek Venkatraman Krishnan acknowledges financial support from the European Research Council (ERC) starting grant ‘COMPACT’ (grant agreement number: 101078094). Alessandro Ridolfi is supported by the Italian National Institute for Astrophysics (INAF) through an ‘IAF - Astrophysics Fellowship in Italy’ fellowship (Codice Unico di Progetto: C59J21034720001; Project ‘MINERS’). We also give our sincere thanks to Huanchen Hu for her comments on this article.

References

- Bachetti, M., Harrison, F. A., Walton, D. J., et al. 2014, *Nature*, 514, 202
 Bailes, M., Jameson, A., Abbate, F., et al. 2020, *PASA*, 37, e028
 Barr, E. D. 2018, in *Pulsar Astrophysics the Next Fifty Years*, ed. P. Weltevrede, B. B. P. Perera, L. L. Preston, & S. Sanidas, Vol. 337, 175–178
 Bates, S. D., Lorimer, D. R., & Verbiest, J. P. W. 2013, *MNRAS*, 431, 1352
 Bates, S. D., Thornton, D., Bailes, M., et al. 2015, *MNRAS*, 446, 4019
 Bergeron, P., Wesemael, F., Dufour, P., et al. 2011, *ApJ*, 737, 28
 Berthereau, A., Guillemot, L., Freire, P. C. C., et al. 2023, *A&A*, 674, A71
 Boyles, J., Lynch, R. S., Ransom, S. M., et al. 2013, *ApJ*, 763, 80
 Caiazzo, I., Burdge, K. B., Fuller, J., et al. 2021, *Nature*, 595, 39
 Camilo, F., Lyne, A. G., Manchester, R. N., et al. 2001, *ApJ*, 548, L187
 Carpano, S., Haberl, F., Maitra, C., & Vasilopoulos, G. 2018, *MNRAS*, 476, L45
 Cognard, I., Freire, P. C. C., Guillemot, L., et al. 2017, *ApJ*, 844, 128
 Cordes, J. M. 2004, *ASP Conference Series*, 317, 211
 Cruces, M., Champion, D. J., Li, D., et al. 2021, *MNRAS*, 508, 300
 Damour, T. & Deruelle, N. 1986, *Ann. Inst. Henri Poincaré Phys. Théor.*, 44, 263
 Damour, T. & Taylor, J. H. 1991, *ApJ*, 366, 501
 Damour, T. & Taylor, J. H. 1992, *Phys. Rev. D*, 45, 1840
 Deller, A. T., Boyles, J., Lorimer, D. R., et al. 2013, *ApJ*, 770, 145
 Edwards, R. T. & Bailes, M. 2001, *ApJ*, 553, 801
 Edwards, R. T., Hobbs, G. B., & Manchester, R. N. 2006, *MNRAS*, 372, 1549
 Faulkner, A. J., Stairs, I. H., Kramer, M., et al. 2004, *MNRAS*, 355, 147
 Fonseca, E., Cromartie, H. T., Pennucci, T. T., et al. 2021, *ApJ*, 915, L12
 Freire, P. C. C. & Wex, N. 2010, *MNRAS*, 409, 199
 Gaia Collaboration, Prusti, T., de Bruijne, J. H. J., et al. 2016, *A&A*, 595, A1
 Gaia Collaboration, Vallenari, A., Brown, A. G. A., et al. 2023, *A&A*, 674, A1
 Gautam, T., Freire, P. C. C., Batrakov, A., et al. 2022, *A&A*, 668, A187
 Gregoris, D. & Ong, Y. C. 2023, *Annals of Physics*, 452, 169287
 Guo, Y. J., Freire, P. C. C., Guillemot, L., et al. 2021, *A&A*, 654, A16
 Hobbs, G., Manchester, R. N., Dunning, A., et al. 2020, *PASA*, 37, e012
 Hobbs, G. B., Edwards, R. T., & Manchester, R. N. 2006, *MNRAS*, 369, 655
 Hollands, M. A., Tremblay, P. E., Gänsicke, B. T., et al. 2020, *Nature Astronomy*, 4, 663
 Hotan, A. W., van Straten, W., & Manchester, R. N. 2004, *PASA*, 21, 302
 Hu, H., Kramer, M., Wex, N., Champion, D. J., & Kehl, M. S. 2020, *MNRAS*, 497, 3118
 Israel, G. L., Belfiore, A., Stella, L., et al. 2017, *Science*, 355, 817
 Jacoby, B. A., Bailes, M., Ord, S. M., Knight, H. S., & Hotan, A. W. 2007, *ApJ*, 656, 408
 Jacoby, B. A., Chakrabarty, D., van Kerkwijk, M. H., Kulkarni, S. R., & Kaplan, D. L. 2006, *ApJ*, 640, L183
 Jonas, J. & MeerKAT Team. 2016, in *MeerKAT Science: On the Pathway to the SKA*, 1

- Kaplan, D. L., Boyles, J., Dunlap, B. H., et al. 2014, *ApJ*, 789, 119
- Knispel, B., Eatough, R. P., Kim, H., et al. 2013, *ApJ*, 774, 93
- Kopeikin, S. M. 1996, *ApJ*, 467, L93
- Kramer, M., Stairs, I. H., Venkatraman Krishnan, V., et al. 2021, *MNRAS*, 504, 2094
- Krishnakumar, M. A., Maan, Y., Joshi, B. C., & Manoharan, P. K. 2019, *ApJ*, 878, 130
- Külebi, B., Jordan, S., Nelan, E., Bastian, U., & Altmann, M. 2010, *A&A*, 524, A36
- Kundu, A. & Mukhopadhyay, B. 2012, *Modern Physics Letters A*, 27, 1250084
- Lazarus, P., Tauris, T. M., Knispel, B., et al. 2014, *MNRAS*, 437, 1485
- Löhmer, O., Mitra, D., Gupta, Y., Kramer, M., & Ahuja, A. 2004, *A&A*, 425, 569
- Lorimer, D. R., Faulkner, A. J., Lyne, A. G., et al. 2006, *MNRAS*, 372, 777
- Lorimer, D. R. & Kramer, M. 2005, *Handbook of pulsar astronomy* (Cambridge University press)
- Martinez, J. G., Gentile, P., Freire, P. C. C., et al. 2019, *ApJ*, 881, 166
- Martinez, J. G., Stovall, K., Freire, P. C. C., et al. 2015, *ApJ*, 812, 143
- Mathew, A. & Nandy, M. K. 2021, *Royal Society Open Science*, 8, 210301
- McKee, J. W., Freire, P. C. C., Berezina, M., et al. 2020, *MNRAS*, 499, 4082
- McMillan, P. J. 2017, *MNRAS*, 465, 76
- Mickaliger, M. B., Lorimer, D. R., Boyles, J., et al. 2012, *ApJ*, 759, 127
- Miller, D. R., Caiazzo, I., Heyl, J., et al. 2023, *ApJ*, 956, L41
- Oswald, L. S., Karastergiou, A., Posselt, B., et al. 2021, *MNRAS*, 504, 1115
- Özel, F. & Freire, P. 2016, *ARA&A*, 54, 401
- Pallanca, C., Lanzoni, B., Dalessandro, E., et al. 2013, *ApJ*, 773, 127
- Parent, E., Kaspi, V. M., Ransom, S. M., et al. 2019, *ApJ*, 886, 148
- Poutanen, J., Lipunova, G., Fabrika, S., Butkevich, A. G., & Abolmasov, P. 2007, *MNRAS*, 377, 1187
- Prša, A., Harmanec, P., Torres, G., et al. 2016, *AJ*, 152, 41
- Pshirkov, M. S., Dodin, A. V., Belinski, A. A., et al. 2020, *MNRAS*, 499, L21
- Radhakrishnan, V. & Cooke, D. J. 1969, *Astrophys. Lett.*, 3, 225
- Rickett, B. J. 1977, *ARA&A*, 15, 479
- Ridolfi, A., Freire, P. C. C., Gupta, Y., & Ransom, S. M. 2019, *MNRAS*, 490, 3860
- Romani, R. W., Narayan, R., & Blandford, R. 1986, *MNRAS*, 220, 19
- Sarkissian, J. M., Carretti, E., & van Straten, W. 2011, in *American Institute of Physics Conference Series*, Vol. 1357, *Radio Pulsars: An Astrophysical Key to Unlock the Secrets of the Universe*, ed. M. Burgay, N. D’Amico, P. Esposito, A. Pellizzoni, & A. Possenti, 351–352
- Shakura, N. I. & Sunyaev, R. A. 1973, *A&A*, 24, 337
- Shamohammadi, M., Bales, M., Freire, P. C. C., et al. 2023, *MNRAS*, 520, 1789
- Shapiro, I. I. 1964, *Phys. Rev. Lett.*, 13, 789
- Shklovskii, I. S. 1970, *Soviet Ast.*, 13, 562
- Splaver, E. M., Nice, D. J., Arzoumanian, Z., et al. 2002, *ApJ*, 581, 509
- Staveley-Smith, L., Wilson, W. E., Bird, T. S., et al. 1996, *PASA*, 13, 243
- Tan, C. M., Bassa, C. G., Cooper, S., et al. 2020, *MNRAS*, 492, 5878
- Tauris, T. M., Kramer, M., Freire, P. C. C., et al. 2017, *ApJ*, 846, 170
- Tauris, T. M., Langer, N., & Kramer, M. 2012, *MNRAS*, 425, 1601
- Tauris, T. M., Langer, N., & Podsiadlowski, P. 2015, *MNRAS*, 451, 2123
- Tauris, T. M. & Sennels, T. 2000, *A&A*, 355, 236
- Tauris, T. M. & van den Heuvel, E. P. J. 2023, *Physics of Binary Star Evolution. From Stars to X-ray Binaries and Gravitational Wave Sources* (Princeton University Press)
- Taylor, J. H. & Weisberg, J. M. 1989, *ApJ*, 345, 434
- Thorsett, S. E., Arzoumanian, Z., McKinnon, M. M., & Taylor, J. H. 1993, *ApJ*, 405, L29
- Thorsett, S. E. & Chakrabarty, D. 1999, *ApJ*, 512, 288
- Tomaschitz, R. 2018, *Physica A Statistical Mechanics and its Applications*, 489, 128
- van den Heuvel, E. P. J. 2019, *IAU Symposium*, 346, 1
- van Haasteren, R., Levin, Y., McDonald, P., & Lu, T. 2009, *MNRAS*, 395, 1005
- van Kerkwijk, M. H. & Kulkarni, S. R. 1999, *ApJ*, 516, L25
- Virtanen, P., Gommers, R., Oliphant, T. E., et al. 2020, *Nature Methods*, 17, 261
- Voisin, G., Cognard, I., Freire, P. C. C., et al. 2020, *A&A*, 638, A24
- Yao, J. M., Manchester, R. N., & Wang, N. 2017, *ApJ*, 835, 29
- Yoon, S. C. & Langer, N. 2005, *A&A*, 435, 967
- Zhao, J., Freire, P. C. C., Kramer, M., Shao, L., & Wex, N. 2022, *Classical and Quantum Gravity*, 39, 11LT01

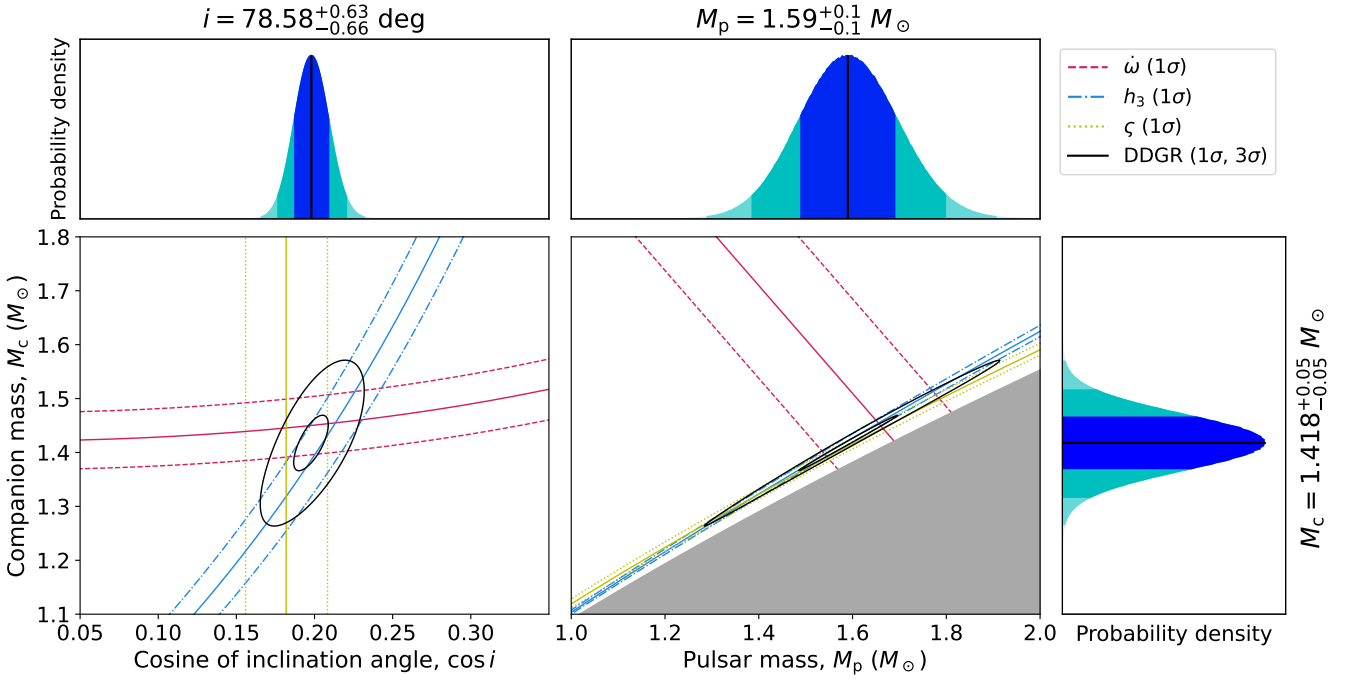
Appendix A: Additional mass constraints plots


Fig. A.1. Mass and inclination angle constraints from the DDH PK measurements and the χ^2 mapping with the DDGR model, both from the global fit and under the assumption of the **Ls** noise model (Table 2). Contours have been drawn following the same principles as in Fig. 5.

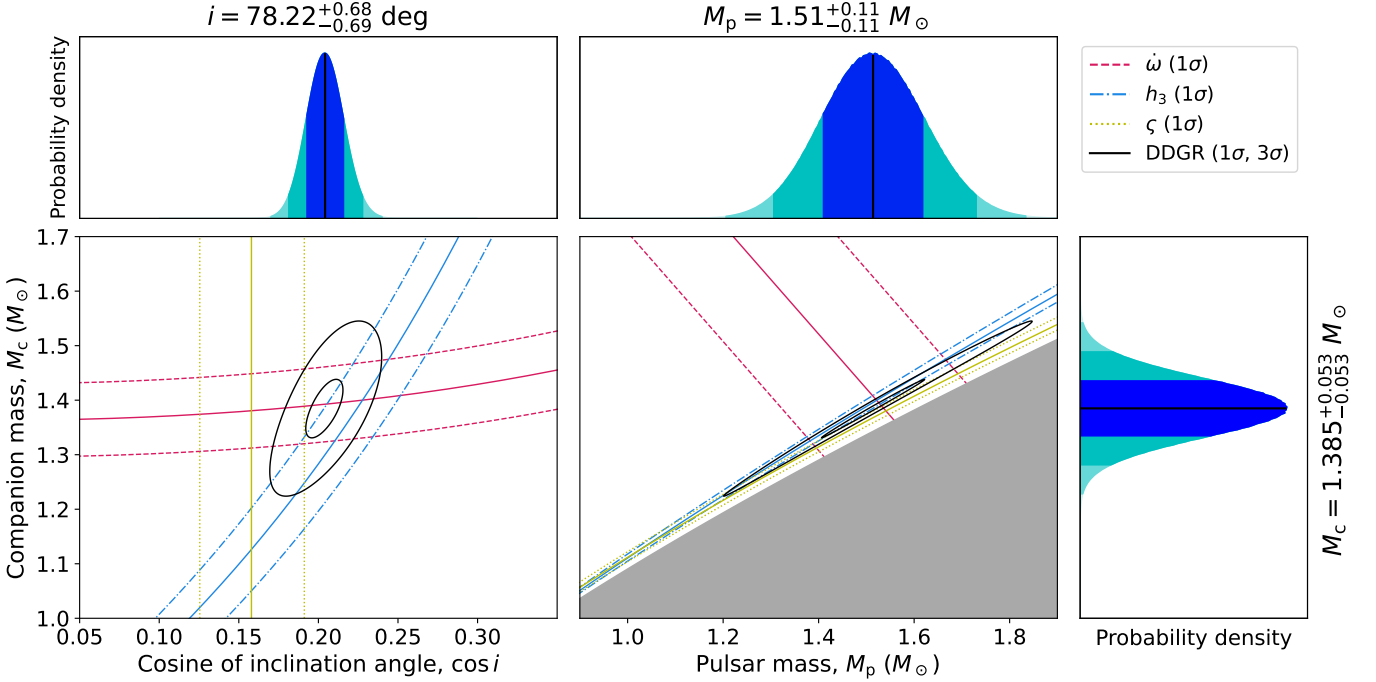


Fig. A.2. Mass and inclination angle constraints from the DDH PK measurements and the χ^2 mapping with the DDGR model, both from the global fit and under the assumption of the **VCs** noise model (Table 2). Contours have been drawn following the same principles as in Fig. 5.

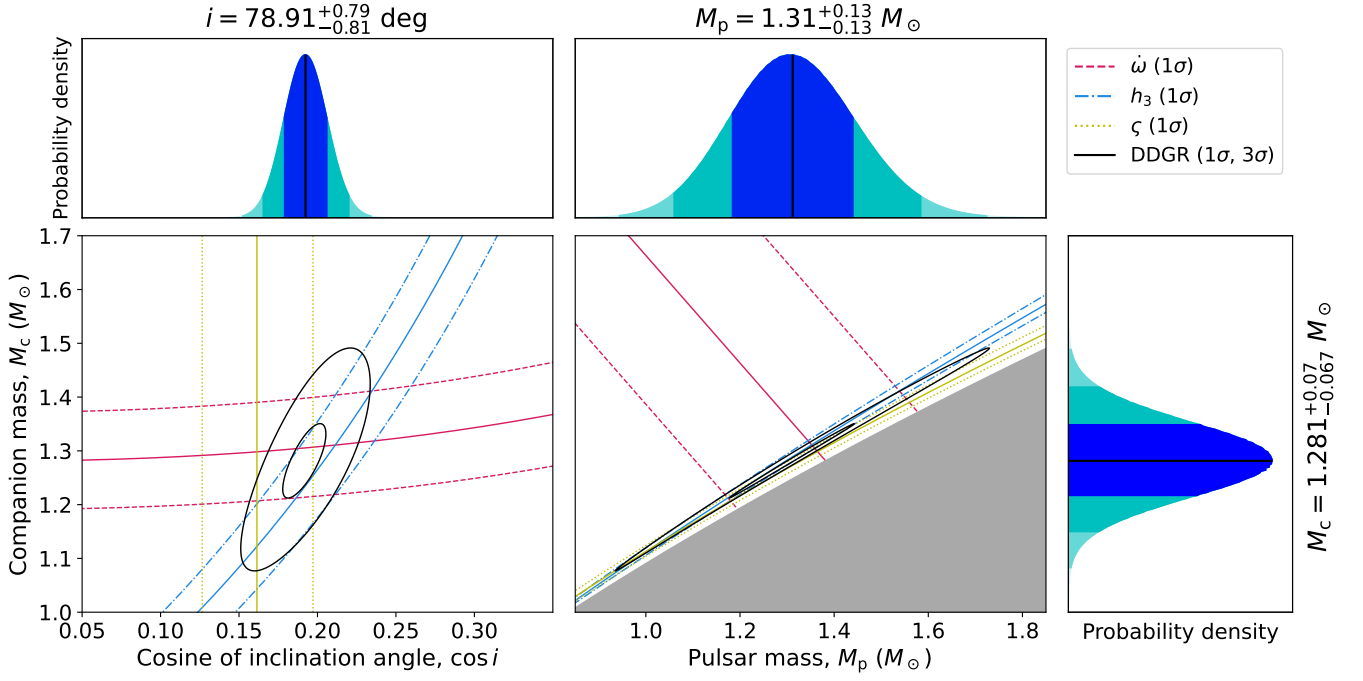


Fig. A.3. Mass and inclination angle constraints from the DDH PK measurements and the χ^2 mapping with the DDGR model, both from the MeerKAT+UWL fit and under the assumption of the VCs noise model (Table 2). Contours have been drawn following the same principles as in Fig. 5.

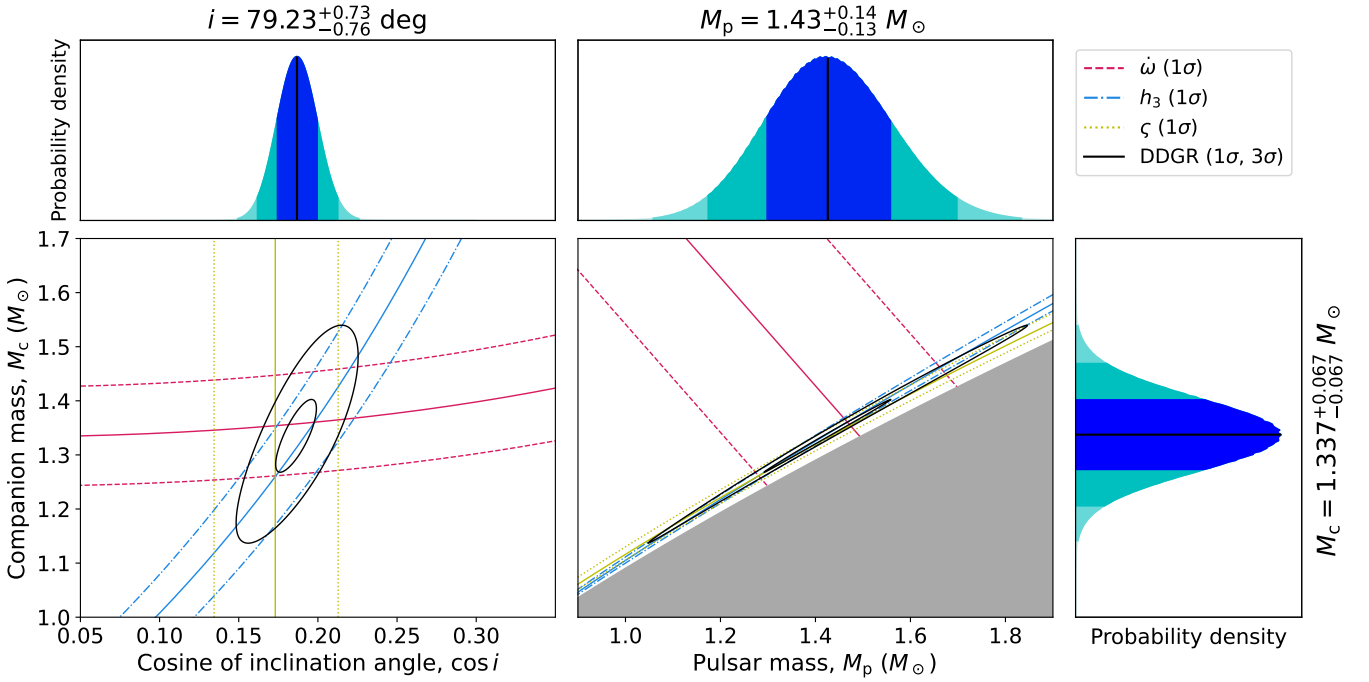


Fig. A.4. Mass and inclination angle constraints from the DDH PK measurements and the χ^2 mapping with the DDGR model, both from the MeerKAT+UWL fit and under the assumption of the Ls noise model (Table 2). Contours have been drawn following the same principles as in Fig. 5.

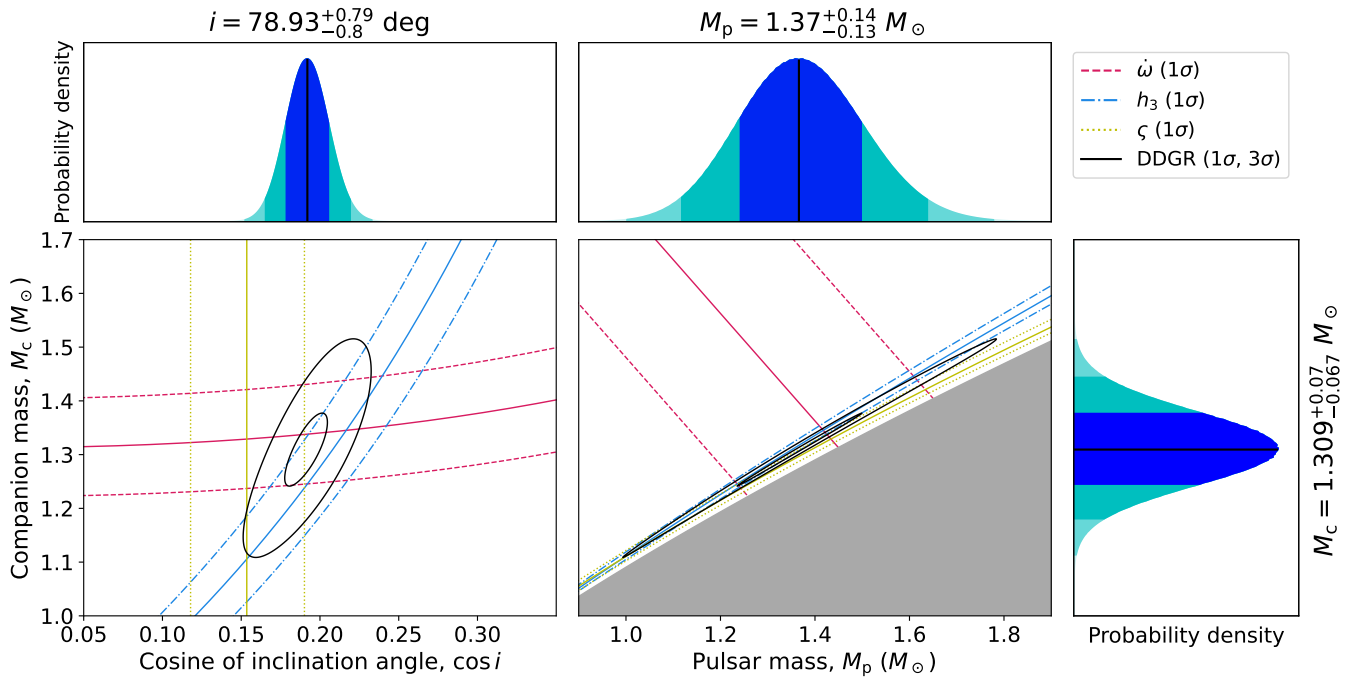


Fig. A.5. Mass and inclination angle constraints from the DDH PK measurements and the χ^2 mapping with the DDGR model, both from the MeerKAT+UWL fit and under the assumption of the Cs noise model (Table 2). Contours have been drawn following the same principles as in Fig. 5.